D Moseev et al.

Fast ion diagnostics in fusion plasmas

Fast ion diagnostics in fusion plasmas

D. Moseev · **M. Garcia-Muñoz** · **B. Geiger** ·
M. Nocente · **M. Salewski**

Abstract On the road to a fusion reactor, a thorough control of the fast ion distribution plays a crucial role. Fusion born alpha particles are, indeed, a necessary ingredient for self-sustained burning plasmas. Recent developments in the diagnostic of the fast ion distribution have significantly improved our predictive capabilities towards future devices. Here we review the state-of-the-art of key diagnostic techniques for confined and lost fast ions. We discuss neutron and gamma-ray spectroscopy, fast ion D (H)-α spectroscopy, collective Thomson scattering, neutral particle analyzers, and fast ion loss detectors. The review covers physical principles of each diagnostic, basic

D. Moseev
Max-Planck-Institut fuer Plasmaphysik
Greifswald, Germany
E-mail: dmitry.moseev@ipp.mpg.de

M. Garcia-Muñoz
University of Seville
Seville, Spain
E-mail: mgm@us.es

B. Geiger
Max-Planck-Institut fuer Plasmaphysik
Greifswald, Germany
E-mail: benedikt.geiger@ipp.mpg.de

M. Nocente
Dipartimento di Fisica "G. Occhialini", Universita di Milano-Bicocca
Milano, Italy and
Istituto di Fisica del Plasma "P. Caldirola", Consiglio Nazionale delle Ricerche
Milano, Italy
E-mail: —massimo.nocente@mib.infn.it

M. Salewski
Technical University of Denmark
Kgs. Lyngby, Denmark
E-mail: msal@fysik.dtu.dk

setups, operational parameters, and the sensitivity. Lastly, we discuss integrated data analysis of fast-ion diagnostics by velocity-space tomography which allows measurements of 2D velocity distribution functions of confined fast ions.

Keywords diagnostics · Fast Ions · Fusion plasmas

1 Introduction

Fast ions are a crucial ingredient of a burning fusion plasma as they constitute an essential source of energy to heat the plasma and thus to sustain the fusion burn. They are also significant sources of momentum and current in tokamak plasmas. In present fusion devices, the main fast-ion sources are Neutral Beam Injectors (NBI) and Ion Cyclotron Resonance Heating (ICRH) systems. In a fusion plasma, the main fast-ion source will be fusion reactions, especially generating α particles at 3.5 MeV.

However, there are several transport mechanisms that can lead to a fast-ion redistribution and eventually loss before they have slowed down to the plasma bulk through Coulomb collisions [56, 30]. A fast-ion redistribution is typically accompanied by a degradation of the fast-ion heating and current drive efficiency and thus of the fusion reactor performance. If sufficiently intense and localized, a fast-ion loss may even damage the integrity of the first wall of the device [25]. Magnetohydrodynamic (MHD) fluctuations are the main cause of fast-ion transport [40]. Among others, Alfven Eigenmodes (AEs) [180, 58, 79, 5, 154, 157, 159, 174, 44], Neoclassical Tearing Modes (NTMs) [187, 15, 39], Sawtooth crashes [87, 175, 147] and Edge Localized Modes (ELMs) [45, 46] can reduce the fast-ion density by up to 50% of the classically expected density. The wave-particle interaction causing this fast-ion transport depends on the nature of the fluctuations and fast-ion orbital characteristics. In order to better understand the physics mechanisms underlying the observed MHD induced fast-ion transport, accurate time-resolved measurements of the fast-ion distribution in phase-space are needed. Such measurements are essential to validate and challenge present theories, which advances our understanding and predictive capabilities towards future fusion devices. The harsh environment present in a fusion device complicates this task. Recent breakthroughs in the diagnostic of confined and lost fast-ions have allowed measurements of MHD induced fast-ion transport with an unprecedented level of detail and accuracy.

In this review, the state-of-the-art of key fast-ion diagnostic techniques in fusion plasmas is presented together with a brief discussion of their prospects for future devices. The physics of energetic ions has been discussed in several review papers [55, 56, 68, 30, 130, 155], and, after decades of research, is still incomplete. Here we do not discuss the physics of fast ions, but focus on their diagnostic, which has proven to be a challenging topic by itself.
It is of interest to measure fast ions that are confined in the plasma by the magnetic field as well as fast ions that are lost from the plasma. The most common diagnostics for confined fast ions are neutron emission spectroscopy (NES) or the simpler neutron counters, γ-ray spectroscopy (GRS), fast ion D_α spectroscopy (FIDA), neutral particle analyzers (NPA), and collective Thomson scattering (CTS). Fast ion loss detectors (FILD) measure fast ions that are ejected from the plasma either due to

the birth on unconfined orbits or due to the interaction with the plasma and waves therein. The different fast-ion diagnostics probe various parts of the phase space with different sensitivities and thus provide complementary information about the fast-ion phase space distribution function.

We may divide the confined ion diagnostics into two main groups. The active measurements require the injection of a beam, either radiation or particles, and the measured signal depends on parameters of the plasma and of this injected beam. For example, the NBI required for FIDA and active NPA is often a part of the heating scenario, so that these diagnostics are practically non-perturbative. If the beam is not used for heating, short pulses of the probe NBI need to be injected. The probe beam for CTS consists of unabsorbed mm-wave radiation with a frequency between or below the electron cyclotron emission harmonics.

In passive measurements one monitors radiation or particles naturally emitted by the plasma, and hence they never perturb the plasma. Typical examples of the passive fast ion diagnostics are NES, neutron counters, GRS, and passive NPA. In GRS one measures the energy spectrum of γ-rays originating from fusion reactions. In NES one detects neutrons originating from fusion reactions and measures, depending on the type of the detector, a variety of quantities that can be related to the neutron energies. In passive NPAs one measures the escaping neutral particles that have been generated in a charge-exchange reaction.

The division into active and passive diagnostics is reflected in the achievable spatial resolution of the measurements. The probe beam of the active measurements and the line-of-sight of the detector are arranged to intersect at the desired measurement location in the plasma. The spatial resolution of the active measurements is therefore largely determined by the sizes of the probe beam and the line-of-sight and by their intersection angle. For FIDA and NPA, the lines-of-sight can be chosen to be narrow, whereas the size of the heating beam is determined by the desired heating performance rather than the diagnostic needs. Microwave-based CTS usually uses the available infrastructure of the ECRH system. The sizes of the beams depend on the propagation of the microwaves through the plasma and the geometry of the diagnostic setup.

The passive diagnostics NES, GRS and passive NPAs always measure along their entire line-of-sight. Nevertheless, the measurement can be strongly dominated by only parts of the line-of-sight. The gamma-ray and neutron emission is strongest in the plasma center and weakens substantially towards the plasma edge. In contrast to that, passive NPAs have a strong contribution from the plasma edge where there are high densities of donor neutrals. This spatial weighting can act as practical spatial resolution. Gamma-rays and neutrons at JET are monitored along several lines-of-sight such that their 2D emission profiles in the poloidal plane can be found by tomographic inversion.

The fast ion loss detector (FILD) is a charged particle collector located in the direct proximity of the plasma edge. It measures the flow of charged particles. In contrast to the diagnostics of confined fast ions, the FILD diagnostic measures energy and pitch of the detected particles on the scintillator plate directly. The original orbit of the detected particles can be restored from the orbit-following simulations. The

diagnostic is compact and is often installed on a manipulator. By moving the detector on the manipulator, different plasma volumes can be probed.

The velocity-space sensitivities of the confined fast ion diagnostics have only very recently been understood and quantified. The velocity-space observation regions depend on the diagnostic principle and the gyro-motion of the energetic particles. Often one can draw conclusions on the velocity component along the line-of-sight of the diagnostic from the detected signal. High-energy detections (frequency upshift for radiation) indicate motion of the energetic particle towards the detector whereas low-energy detections indicate motion away from the detector. For two-step reactions emitting γ-rays this is not strictly true but there is still a bias in this direction.

The paper is organized as following: Section 2 describes the NES and GRS diagnostics; the charge exchange based diagnostics, NPA and FIDA, are explained in Section 3; Section 4 is devoted to CTS. The diagnostic for lost ions, FILD, is described in Section 5. Section 6 discusses velocity-space tomography as tool for integrated data analysis of the available measurements. Section 7 concludes the paper.

2 Neutron emission and gamma-ray spectrometry

In this section we review diagnostics based on the measurements of various nuclear reaction products originating from the high-temperature plasmas. Up to now, this is the most mature family of diagnostics. It is present in different forms on most of the current fusion experiments.

2.1 Physics principles

Neutron measurements Neutron emission arises from fusion reactions of the plasma constituents, most notably the $d(d,n)^3He$ and $t(d,n)^4He$ reactions in plasmas of deuterium (D) and deuterium-tritium (DT), respectively. Neutron measurements were originally intended as a way to determine the fusion power yield as well as its profile. With the advent of auxiliary heating systems delivering powers in the MW range - and therefore the presence of a significant fast ion content in the plasma - neutron measurements were later also applied in studies of suprathermal fuel ions. At a fundamental level, fast ions generate a neutron population with energies exceeding those expected from a purely thermal plasma. This follows from the application of energy and momentum conservation to the $d(d,n)^3He$ and $t(d,n)^4He$ fusion reactions and is mathematically expressed by an equation relating the neutron energy E_n to the known motional state of the reactants [14]

$$E_n = \frac{1}{2}m_n V_{cm}^2 + \frac{m_n}{m_n + m_f}(Q+K) + V_{cm}\cos\theta\left(\frac{2m_n m_f}{m_n + m_f}(Q+K)\right)^{1/2} \quad (1)$$

Here m_n and m_f indicate the masses of the neutron and the second product of the fusion reaction, respectively. $\mathbf{V_{cm}} = (m_1\mathbf{v_1} + m_2\mathbf{v_2})/(m_1 + m_2)$ and $K = 1/2\mu v_{rel}^2$ are the center of mass (c.m.) velocity and relative kinetic energy of the two reactant ions, described by their masses m_1 and m_2 and velocities $\mathbf{v_1}$ and $\mathbf{v_2}$. $\mathbf{v_{rel}} = \mathbf{v_2} - \mathbf{v_1}$ is the
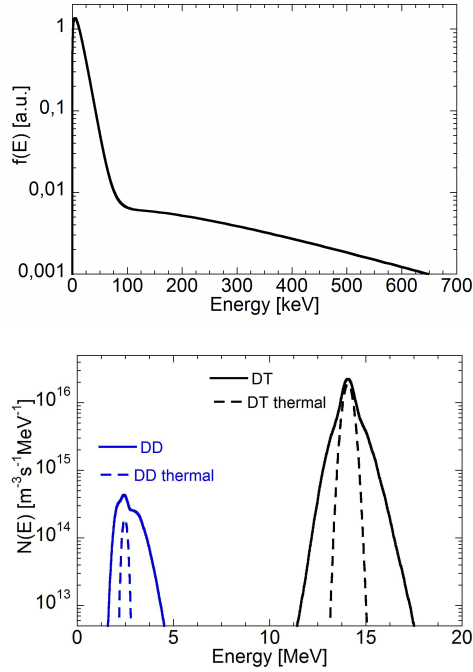
Fig. 1 (left) Fuel ion distribution function with external heating. We assume that the plasma has $T_i = 10$ keV bulk ion temperature and $n = 10^{20}$ m^{-3} density. A 0.01% fraction of the fuel ion is driven to a tail temperature of 200 keV by the auxiliary heating. (right) Expected neutron spectrum produced in DD and DT plasmas by reactions among ions described by the distribution function shown to the left as calculated by the GENESIS code [116, 172] (solid lines). For comparison, the neutron spectrum expected from bulk fuel ions at thermal equilibrium and with $T_i = 10$ keV is also shown by dashed lines.

relative velocity and θ indicates the angle between $\mathbf{V_{c.m.}}$ and the neutron velocity vector in the c.m. frame, which depends on the angle between the line-of-sight of the diagnostic and the magnetic field.

For purely thermal plasmas, the neutron spectrum that is calculated from equation 1 is approximately Gaussian with a width proportional to the square root of the ion temperature [31]. The center of the spectrum is at 2.5 MeV and 14 MeV for $d(d,n)^3$He and $t(d,n)^4$He neutrons, respectively.

Deformations of the Gaussian shape with the appearance of tails at both ends of the spectrum occur whenever the fuel ion distribution function has suprathermal components, for example as a consequence of neutral beam or radio-frequency heating. Figure 1 shows a calculation of the neutron spectrum produced by fusion reactions among ions described by the distribution function displayed to the left. We assume that neutrons are observed along an orthogonal line-of-sight with respect to the magnetic field direction. The fuel ions are here described by a Maxwellian distribution with $T_i = 10$ keV temperature and a density of $n = 10^{20}$ m^{-3}. The addition of a suprathermal ion population has an assumed tail temperature of 200 keV and a relative density as little as 0.01%, which is here used as a mock up of the effects of the

injection of radio-frequency waves on the fuel ion distribution function. We also separately consider the corresponding signatures in the neutron spectrum from deuterium (D) and deuterium-tritium (DT) plasmas. In both cases, tails appear at both ends of the spectrum. Experimentally, however, it is only the high energy tail that can be used for diagnostic applications as the low energy signature is often altered by scattered neutrons (see section 2.2). Fast ion studies by neutron spectroscopy therefore detect the high energy tail in the spectrum by use of suitable instruments (see 2.2). The magnitude of the supra-thermal ion effects in the neutron spectrum is very different for D and DT plasmas. In the former case, a fast ion population often leads to a significant enhancement of the neutron rate, as the cross section of the $d(d,n)^3He$ reaction is a monotonic function of energy up to about 1 MeV in the c.m. frame [117]. In the latter case, instead, there is certainly a modification of the shape of the spectrum, but the enhancement of the reactivity is more modest, mostly because fast ions with energies exceeding that of the resonance in the cross section (≈ 70 keV in the c.m. frame) add little to the neutron yield.

Although the dominant fast ion application of neutron measurements is to determine the effect of the heating systems on the fuel deuterium and tritium, in some special cases non-fuel energetic ions can also lead to a tail in the neutron spectrum. This occurs because the fuel ion distribution function is distorted at high energies (say, > 100 keV) when fast non-fuel ions in the MeV range collide elastically on the fuel ions as they slow down in the plasma[121]. A notable application is the possibility to measure the α particle distribution function by the observation of low amplitude ($\approx 10^{-4}$), high energy tails in the neutron spectrum. These are born from the so-called α knock-on process, i.e. (mostly) head-on nuclear elastic scattering collisions between α particles in the MeV range and fuel ions. The α knock-on tail has been used to assess classical slowing down of the α particles in DT experiments at JET[76] by means of a dedicated neutron detector with high dynamic range sensitivity (see section 2.2).

Besides spectrometry, neutron profile measurements can also contribute to fast fuel ion studies. Here the goal is to measure changes of the neutron profile induced by fast ion driven instabilities in the plasma and which, after careful modelling, can be related to a redistribution of the ions leading to neutron emission. Typically, neutron profile measurements are used especially to measure modifications of the neutron emission in response to sawteeth and fishbones effects on the fast ions, mostly in D plasmas [20].

Gamma-ray measurements Gamma-ray measurements are emerging as an essential tool to study fast ion physics in the MeV range [81,83,173]. The reactions leading to gamma-ray emission can be divided into two categories, namely one-step and two-step processes. In one-step reactions. i.e. those of the type $a(b,\gamma)c$, the two light nuclei a and b merge together to form the heavier nucleus c. The excess energy that comes from the mass difference $m_a + m_b - m_c$ is released as a gamma-ray. Notable examples are the weak counterparts ($\approx 10^{-5}$ less probability) of the main $d(d,n)^3He$ and $t(d,n)^4He$ fusion reactions, i.e. $d(d,\gamma)^4He$ and $t(d,\gamma)^5He$, respectively.

Two-step reactions instead involve a fast ion f and an impurity i. In the first stage,

the fast ion reacts with the impurity to produce a heavy nucleus N and a light product p, i.e. i(f,p)N. Impurities are often found naturally in fusion devices, as they arise from erosion of the materials used in the first wall, but can also be injected on purpose by pellets or evaporation. In some cases, N can be born in an excited nuclear state that, on a time scale of some picoseconds or less, de-excites with the emission of gamma-ray radiation (second step). If the gamma-ray is detected, it can be used to infer information on the fast ion that started the two-step process. A notable example is here the $^9\mathrm{Be}(\alpha,n)^{12}\mathrm{C}^*$ reaction, where $^{12}\mathrm{C}$ born on its first excited state emits a gamma-ray at a characteristic energy of 4.44 MeV when the reaction is initiated by α particles in a fusion reactor.

Historically, one-step gamma-ray reactions were the first to be proposed for diagnostic purposes around 1980s but as for neutron measurements, they were initially intended as a means to derive the bulk ion temperature T_i in the plasma core rather than for fast ion applications [21]. In this case, T_i can in principle be derived from the broadening of the γ ray peak shape or from its shift with respect to its nominal energy $E_\gamma = (m_a + m_b - m_c) \cdot c^2$. In practice, as fusion neutron diagnostics developed, neutrons soon became the reference technique to measure core T_i, as neutrons are by far more abundant thanks to the comparably higher production cross sections.

One-step γ-ray reactions are, however, nowadays useful for fast ion measurements, especially when radio-frequency waves are injected in the plasma to accelerate hydrogen. In this case, rather than the $d(d,\gamma)^4\mathrm{He}$ and $t(d,\gamma)^5\mathrm{He}$ reactions, the $d(p,\gamma)^3\mathrm{He}$ [119] and $t(p,\gamma)^4\mathrm{He}$ [80] emissions between fast protons and bulk deuterium or tritium are of relevance in D and DT plasmas, respectively. As for T_i applications, information on the fast proton distribution function resides in the position and shape of the peak. Careful modelling is required to extract quantitative information from the spectral shape as the simple analytical formulas that apply to Maxwellian plasma (see for example [21]) very often break at the typical energies of the fast ions found in present tokamaks [124]. An important advantage for the application of one-step reactions to fast proton studies is a ≈ 100 times higher emission compared to the same reactions among thermal ions, as the cross sections for $d(p,\gamma)^3\mathrm{He}$ and $t(p,\gamma)^4\mathrm{He}$ monotonically increase up to the MeV energy range.

Two-step reactions are even more useful for fast ion applications than one-step reactions for essentially two reasons. Firstly, the cross sections are generally higher by a factor 100 or more. Secondly, there is a large variety of two-step reactions that can occur in a plasma, which implies that different types of fast ions $(p, ^3\mathrm{He}, \alpha$ etc.) can be studied by the two-step gamma-ray emission they produce, even simultaneously. Unlike one-step reactions, which can in principle be used also to extract parameters of the bulk plasma (e.g. core T_i), two-step processes require ions in the MeV range. The cross sections are essentially negligible below a few hundred keV and often have energy thresholds [81]. Information on the fast ions at different levels of detail can be extracted from the measured gamma-ray emission spectrum. At the most basic level, the identification of the mean energy of peaks in the spectrum is used to assess that a specific two-step reaction occurs in the plasma. This in turn establishes that fast ions with energies exceeding that of the reaction threshold must be confined in the plasma. For example, the observation of the 4.44 MeV peak from the $^9\mathrm{Be}(\alpha,n)^{12}\mathrm{C}^*$ reaction indicates that α particles with energies exceeding 1.9 MeV are found in the plasma,

as this is the effective threshold above which the cross section becomes substantial for $^9\mathrm{Be}(\alpha,\mathrm{n})^{12}\mathrm{C}^*$ [120]. At a more detailed level, as for neutrons, modelling of the emission can be performed to extract quantitative information on fast ions from the measurements. Since the heavy nuclei of two-step reactions can be born in several excited states, more than one peak from the same reaction can be emitted by the different possible transitions between the excited states. Examples are the $^{12}\mathrm{C}(^3\mathrm{He},\mathrm{p}\gamma)^{14}\mathrm{N}$ [172] and the $^{12}\mathrm{C}(\mathrm{d},\mathrm{p}\gamma)^{13}\mathrm{C}$ [120] reactions, which have been used to study $^3\mathrm{He}$ and d ions in the MeV range, respectively. In this case, the ratio of peaks from the same reaction depends on the individual cross sections to populate each excited state and its value can change depending on the fast ion energy. An important observation is that the ratio is independent of the fast ion and impurity densities. In practical applications, a model of the fast ion distribution function is used as input to calculate the expected peak ratio for comparison with measurements, for example to determine the tail temperature that best describes fast ions in radio-frequency acceleration experiments. Besides the peak ratio, the measured absolute intensity of the emission can be used to put further constraints on the fast ion energy distribution. This, however, requires an independent measurement of the impurity density, which is often not accurately known.

The most advanced measurement parameter is the shape of the characteristic peaks associated to gamma-ray emission. Figure 2 right shows the 4.44 MeV peak shape from the $^9\mathrm{Be}(\alpha,\mathrm{n})^{12}\mathrm{C}^*$ reaction when the α particle energy distribution is that resulting from classical slowing down by multiple Coulomb collisions, as shown to the left. The calculation was performed with the GENESIS code and shows that the peak has a trapezoidal shape with a full width at half maximum of about 100 keV. This kinematic broadening comes from the fact, as for neutrons, that the excited $^{12}\mathrm{C}$ nucleus produced in the reaction must have an energy spectrum with non-zero width, as described by the $^{12}\mathrm{C}$ analog of equation (1). The corresponding gamma-rays will then be Doppler broadened as they are emitted from nuclei which are not at rest. The detailed relation between the peak shape and the underlying fast ion distribution function is, however, often not straightforward. An important example is the 4.44 MeV peak from $^9\mathrm{Be}(\alpha,\mathrm{n})^{12}\mathrm{C}^*$. For this peak, the shape is representative of 1.9, 2.6 and 4.0 MeV α-particles, but very little sensitive to energies that are intermediate among these values, and also reflects the pitch angle distribution of the alphas. In particular, as the application of weight function formalism (see Section 6) reveals [145], events in the centre of the peak are mostly representative of co- and counter passing ions, while counts at the high and low energy tails of the peak originate from trapped ions. Besides the $^9\mathrm{Be}(\alpha,\mathrm{n})^{12}\mathrm{C}^*$, similar modelling and analysis of the peak shape is nowadays often used to determine the energy distribution of d [28], ^3He [172] and ^4He [120] in experiments based on use of radio-frequency heating to drive ions to the MeV range. At the highest level of detail, knowledge of the peak shape allows measurements of the fast-ion velocity distribution function (see Section 6) [149].

As for neutrons, the spatial profile of gamma-ray emission can also be measured, besides its spectrum. One interest is in this case to simultaneously determine the profiles of different energetic ions in the plasma. This is accomplished by integrating the signal falling in the energy bands associated with the corresponding gamma-ray peaks and by separately determining the profile from counts in each of these bands.
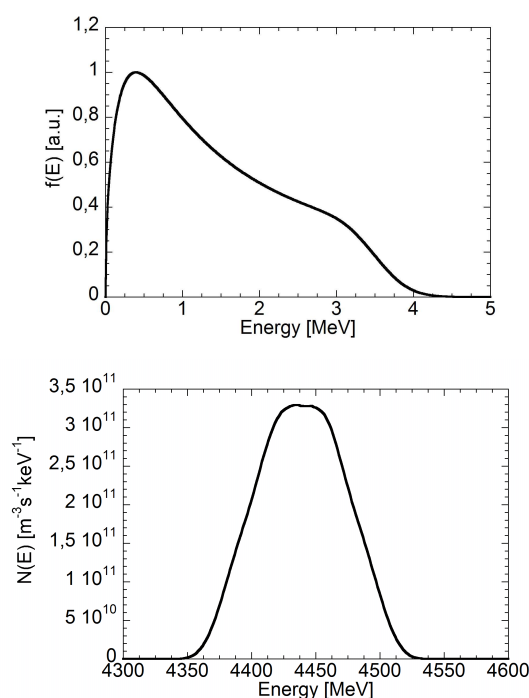
Fig. 2 (left) Classical α particle slowing down distribution function in a plasma with temperature $T_i = T_e = 20$ keV, density $n = 10^{20}$ m^{-3} and 1% beryllium concentration. (right) Spectrum of the 4.44 MeV gamma-ray peak from the ^{9}Be$(\alpha,$n$)^{12}$C* reaction when the α particle distribution function is that shown to the left.

An example is the simultaneous determination of the profile of deuterons and ^4He ions in experiments on radio-frequency heating at multiple harmonics [82]. In this case, a very different profile was obtained by integrating data in the region around the 3.1 MeV and 4.44 MeV peaks from the ^{12}C$($d$,$p$\gamma)^{13}$C and ^{9}Be$(\alpha,$n$)^{12}$C* reactions, respectively, which was explained by the different orbits associated with the ion energies that dominated the emission. Another application is to study the effect of fast ion driven instabilities on the population of energetic ions. A recent application is an experiment where fast changes of the gamma-ray profile were associated to a redistribution of fast ions determined by the onset of toroidal Alfvn eigenmodes in the plasma[48].

2.2 Instrumentation

Neutron measurements As neutrons are uncharged, their detection involves first the (full or partial) conversion of the incoming neutron energy to that of a charged particle, followed by its detection, often by means of a scintillator. The response function that connects the quantity that is actually measured to the incoming neutron energy can be more or less complicated depending on the specific detection principle and
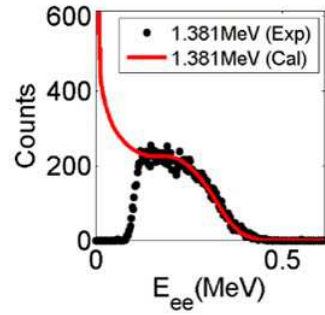
Fig. 3 Pulse height spectrum measured by a EJ301 liquid scintillator detector exposed to monoenergetic 1.381 MeV neutrons. The x axis shows the equivalent electron energy E_{ee}, i.e. the proton energy once the non-linear light yield is taken into account and expressed in terms of electron energies that would give the same light yield. The red curve is the result of a simulation of the expected response. A low energy threshold is used in the measurement to avoid low amplitude noise.

detailed instrument design. For this reason, very different instruments are used depending on the application, where the most significant distinction is often between diagnostic for neutron profile or spectroscopy measurements. In the former case, relatively compact instruments (say, with dimensions of a few cm) are preferred, for practical reasons. In the latter, non-compact spectrometers with dimensions of a few meters are often chosen, as large size can ensure a sufficiently simple response function and extended dynamic range to detect the fast ion features in the spectrum. In recent years, compact detectors have also been proposed for spectroscopy applications, most notably diamond detectors [124], but the quality of the data they can provide does not yet fully compare to that of the dedicated spectrometers. Different instrumental designs are then employed depending on the bulk plasma composition, i.e. D or DT.

 For neutron profile measurements, a very popular detector is the liquid scintillator, which contains a liquid compound of carbon and hydrogen in the scintillation cell. The detection principle is based on nuclear elastic scattering reactions between incoming neutrons and protons of the active material. From classical kinematics, a neutron with energy E_n that scatters off a proton at rest can leave a fraction between zero and its full energy E_n to the proton. The theoretical detector response to monoenergetic neutrons is a square, where the position of the edge represents the incoming neutron energy. In practice, however, no liquid scintillator has a response function as simple as a square, as complicating factors arise. One is that neutron scattering on carbon in the active cell is a competing process. A second, and most important complicating factor, is that it is not the proton energy that is directly measured, but rather the light yield that protons induce as they are stopped in the scintillator material itself. This is often a non-linear function of the proton energy. A third contribution comes from the finite energy resolution of the instrument, which broadens the edge. When all of these are put together, the actual response of the instrument can depart significantly from the ideal square shape (see figure 3). A distinctive feature of liquid scintillators is their capability to discriminate between neutron and gamma-rays by
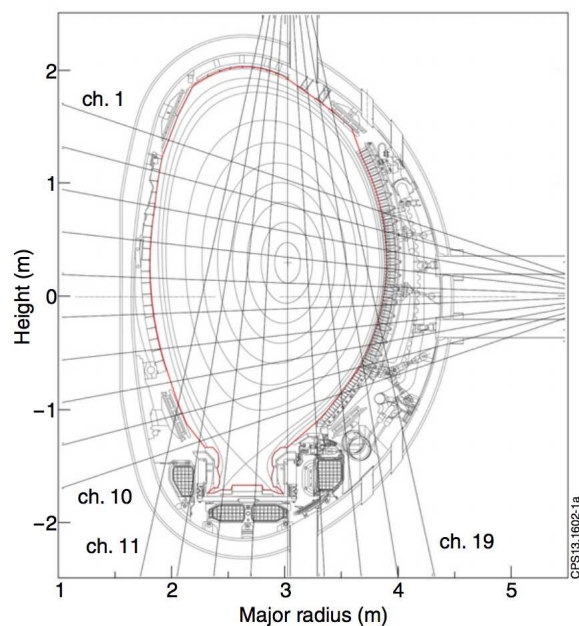
Fig. 4 Sketch of the two JET neutron cameras (vertical and horizontal). The vertical and horizontal lines are the observation chords of each channel of the two camerars. The detectors, not shown in this picture, are put at some distance (about 1.4 m from the first wall at JET) along each chord. The figure is reproduced from [123].

the pulse shape of the signal. This feature is especially important in actual applications, as neutron rich environments are always associated with an equally important gamma-ray background.

Even though some neutron spectroscopy with liquid scintillators has been attempted [185], these detectors are more often used as counters for profile measurements. In this application, a number of liquid scintillators is put at the end of collimated lines of sight to measure the neutron emissivity along each chord (see figure 4). Tomographic inversion techniques with dedicated algorithms [24] are used to reconstruct the local emissivity profile from line integrated measurements. Experimentally, the measurement consists of setting a threshold on each detector and on recording events falling above the threshold. The amplitude of the threshold is chosen so to minimize the extent of scattered neutrons in the recorded signal. These are neutrons that degrade their energy by interactions with the tokamak structures (divertor, first wall etc.) as they travel along their path from the plasma to the instrument (see section 2.3). The extent of scattered neutrons can be especially important for lines of sight that do not explore the plasma core. The stability of the threshold and signal pile up must also be considered. In practice, the dimensions of the detector are chosen so that the counting rate does not exceed about 500 kHz. For higher counting rates, for example those found in DT plasmas, different detectors are preferred. A popular choice is Bicron BC418 [3], which is a plastic scintillator detector with significantly less efficiency to
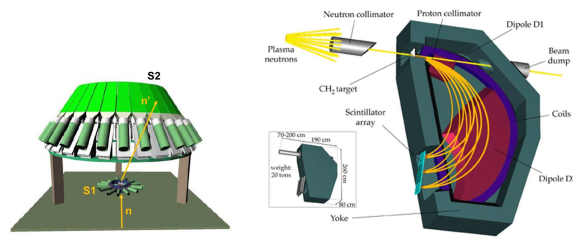
Fig. 5 (left) Schematics of the time-of-flight technique for spectral measurements of neutrons in D plasmas. The neutron beam impinges on a stack of scintillators (S1). Scattered neutrons are recorded by an umbrella of stop detectors (S2). The time-of-flight between scattering in S1 and detection in S2 gives the incoming neutron energy. (right) Schematics of the magnetic proton recoil technique. Elastic scattering of a neutron beam on a polyethylene target produces recoil protons, which are analysed by a magnetic field and dispersed at different energy dependent positions on to a scintillator array. Reproduced with kind permission of Societa Italiana di Fisica. Copyright (C) Societ Italiana di Fisica. Reference: M. Nocente, "Fast-ion measurements with neutron and gamma-ray spectroscopy in thermonuclear plasmas: recent results and future prospects", Nuovo Cimento C, 39 (2016) 289 DOI: 10.1393/ncc/i2016-16289-6.

gamma-ray detection. More recently, synthetic diamond detectors are emerging as a promising technology, especially in view of ITER [17, 18].

When the goal is to measure the high energy tails of the neutron spectrum, such as needed to study the energy distribution of the fast ions, an instrument that provides a significantly simpler response function, improved stability, counting rate capability and higher dynamic range than liquid scintillators is mandatory. To this end, two different techniques are most popular: the time-of-flight (TOF) for deuterium plasmas and the magnetic proton recoil (MPR) for deuterium-tritium plasmas, respectively. In the time-of-flight technique, energy is measured by the time-of-flight of neutrons traveling a known distance. They scatter first on a set of scintillator detectors and are then detected again on a second umbrella of detectors (see Fig. 5 left). The umbrella covers the so-called sphere of constant time-of-flight [38] so that the time-of-flight of the scattered neutrons is a measurement of the incoming neutron energy. The limiting factor are here random coincidences. These are events that appear as coincident within the instrument time acceptance window but come instead from the background, i.e they do not correspond to a neutron that actually travels from the first to the second set of scintillators within the acceptance time window. The rate of random coincidences scales as the square of the neutron rate which limits the maximum counting rate capability of the instrument to up to 500 kHz. This hampers the applications of the TOF technique for DT plasmas where MPR detectors are preferable. Detectors based on TOF are the TOFOR neutron spectrometer at JET [49] and the TOFED instrument at EAST [183, 184]. Fast ion applications include studies of energetic ions produced by neutral beam injection [62] and radio-frequency heating [28, 64], including the effects of sawteeth and toroidal Alfvén eigenmodes on fast ions in the MeV range [48, 63].

The MPR technique is based on a different detection method. Recoil protons produced by neutron scattering are dispersed in a strong magnetic field. In this instrument, neutrons from the plasma scatter in a polyethylene target and produce recoil protons. The recoil protons are momentum analyzed using a large magnet bending
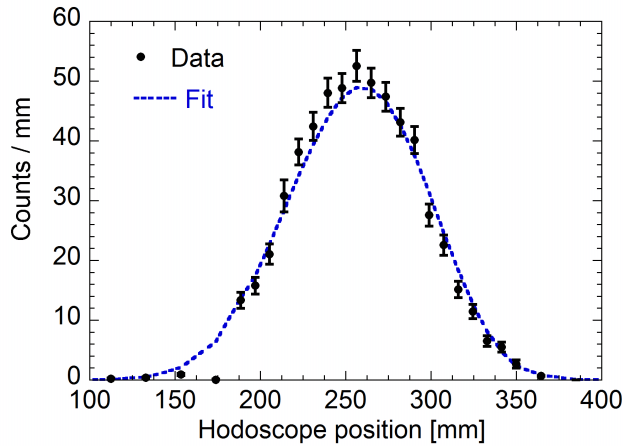
Fig. 6 Neutron spectrum measured by the MPRu magnetic proton recoil spectrometer at JET in a discharge of the Trace Tritium Experiment with deuterium and tritium neutral beam injection. The spectrum is centered at 14 MeV, corresponding to the position at 250 mm on the hodoscope and has a shape determined by reactions between thermal, fast beam ions and their combinations. The solid line is a fit to measured data based on a model of the neutron emission for this discharge. The figure is taken from [123].

their trajectories to different impact positions on a scintillator array (see figure 5 right). The incoming neutron energy spectrum is thus transformed into a position histogram on the array. The thickness of the target is chosen as a compromise between the energy loss of protons within the target and the detection efficiency. The main advantage of this technique is its capability to sustain MHz counting rates. Therefore MPR detectors are especially suitable for applications in high performance DT plasmas, where the extent of random coincidences from the background would be too high for the TOF technique to work. Applications of the MPR to D plasmas are more difficult, mostly because practical values of the polyethylene thickness result in a detection efficiency of about 10^{-4}, which is two orders of magnitude worse than the $\approx 10^{-2}$ of the TOF technique. The MPR principle is employed by the MPRu spectrometer at JET [158]. An example of a neutron spectrum measured with this instrument in a trace tritium experiment at JET is shown in Fig. 6. Fast ion applications of the technique include the important assessment of classical α particle slowing down in the JET 1997 DT experiments by observations of the corresponding knock-on component in the spectrum [76] (see section 2.1). More traditional applications are for studies of beam ion transport in trace tritium plasmas [123] as well as the acceleration of tritium ions by different radio-frequency schemes [171]. Unlike TOF instruments, the use of MPR for extended physics studies has been more limited up to now, mostly because of the significantly shorter availability of plasmas with tritium in present tokamak experiments compared to D plasmas. A common feature of TOF and MPR is that they provide an almost one-to-one correspondence between neutron energy and the quantity that is actually measured (time of flight or position), which greatly simplifies the analysis and adds to the stability of the detector. Still, a detailed
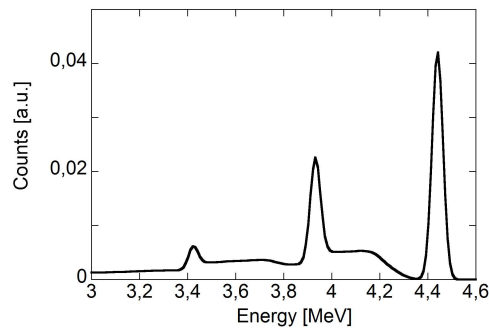
Fig. 7 MCNP simulation of the gamma-ray spectrum recorded by a 3"x6" (diameter x height) LaBr$_3$ detector when exposed to 4.44 MeV gamma-rays. The spectrum shows the full energy peak at 4.44 MeV, as well as the single and double escape peaks [86] at 4.44 - 0.511 MeV and 4.44 - 1.022 MeV, respectively, resulting from pair production in the detector. The continuum is due to Compton interactions. An energy resolution of 3.1% at the 662 keV line from ^{137}Cs is assumed .

knowledge of the instrument response function is mandatory to extract quantitative information [72].

Gamma-ray measurements The detection of gamma-rays is comparably simpler than the detection of neutrons and involves the conversion of the radiation energy of one or more electrons which are subsequently stopped in the detector material. The conversion can proceed via the photoelectric, Compton and pair production processes or, in most cases, a combination of them [86]. The relative importance of the three processes depends on the detector size and detailed geometry. Figure 7 shows a typical response function in the case of a E_0 =4.44 MeV gamma-ray from the ^{9}Be$(\alpha,$n$)^{12}$C* reaction that impinges on a 3"x6" LaBr$_3$ crystal. The signature of the different concurring processes is seen as the appearance of peaks due to the photoelectric effect (at E_0) and pair production (at E_0-0.511 MeV and E_0-1.022 MeV). These sit on a continuous structure that comes from Compton interactions. In addition, there can then be an instrumental broadening of each channel of the spectrum, the magnitude of which mostly depends on the detector material. The broadening of the full energy peak from a calibration source with a well defined energy (for example 662 keV from ^{137}Cs) defines the instrumental resolution at that energy.

 Unlike neutron spectroscopy, it is often not the overall shape of the spectrum that is used for fast ion studies by gamma-ray spectroscopy, but only the full energy peak. As mentioned in section 2.1, experimentally the detection of fast ions by gamma-ray emission consists of identifying the reactions that can lead to the measured peaks, of analysing their intensities and ratios and, in the most advanced applications, of measuring their detailed shape. For this reason, large detectors (a few inches diameter by a few inches length) that maximise the probability of a photoelectric interaction are chosen. In terms of detector type, the most popular choice are inorganic scintillators. Initially, NaI(Tl) and BGO were used [81,83], mostly because of their large availability in the field of applied nuclear physics and since they provided a reasonable compromise between detection efficiency and energy resolution. Nowadays,
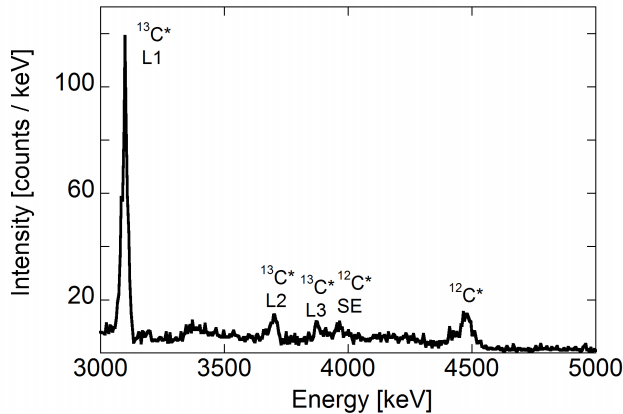
Fig. 8 Gamma-ray spectrum measured with a High Purity Germanium detector in a discharge with 3rd harmonic ion cyclotron heating of ^{4}He ions at JET with a carbon wall. The full and single escape peaks produced by gamma-rays born in the ^{9}Be(^{4}He,n)^{12}C reaction between fast ^{4}He ions and ^{9}Be impurities injected with overnight evaporation are seen. There are also full energy peaks produced by the de-excitation of the first, second and third excited states of ^{13}C born from the ^{12}C(d, p)^{13}C reaction between fast deuterons and ^{12}C impurities. In all cases, a clear fast ion Doppler broadening of each line is seen. The figure is taken from [120].

new, improved inorganic scintillators have emerged that are to replace the previous detectors. A notable example is LaBr$_3$ [118], which offers a factor ≈ 2 better energy resolution than NaI (3.1% compared to 7% at 662 keV) and a decay time as fast as 30 ns, which opens up to gamma-ray spectroscopy at MHz counting rates [122]. Such counting rates are mandatory for applications to high power DT plasmas. Since its installation at JET, LaBr$_3$ with preferred dimensions of 3"x6" and a $\approx 30\%$ full energy peak efficiency has now become the reference choice also in view of ITER [126, 23]. When analysis of the fine peak shape is the aim of the measurement, a detector which offers a virtually zero line instrumental broadening is desired. High purity germanium (HpGe) detectors [172], which are based on collecting the large number of electron-hole pairs generated by the interaction of gamma-rays with the active material, are here the natural choice. An instrumental broadening of ≈ 0.1 keV is easily achievable for emission lines in the MeV range with these detectors. This instrumental broadening is negligible compared with typical values of the Doppler broadening around 100 keV and makes the measured line shape representative of the fast ion motion only. An example of a gamma-ray spectrum measured in a radio-frequency heating experiment at JET with HpGe is shown in Fig. 8. Disadvantages of HpGes compared with LaBr$_3$ are that they must be cooled, they have about 4-5 times less detection efficiency for practical detector dimensions and, even if they were demonstrated to work up to ≈ 1 MHz, they have a limited throughput as the counting rate approaches some hundreds of kHz[176]. In practice, in modern installations, most often both LaBr$_3$ and HpGe are available on the same line-of-sight, and a selection on which detector to use is made on a case by case basis.

Cylindrical detectors with a diameter and length of a few inches as those described so

far can also be used for gamma-ray profile measurement. This is the approach envisaged for ITER [126]. However, in existing tokamaks, for example at JET, gamma-ray detectors were developed at a later stage than those for neutrons. γ-ray profile capabilities were added to an already existing neutron camera. For this reason, space limitation turns out to be an important issue. The reason is mostly related to the need to shield the photomultiplier tube of the scintillators from the magnetic field, which is fairly large at the neutron camera location. This would require a combination of mu metal and a few centimetres of soft iron, but this is not possible in practice due to the limited space available. The actual implementation is therefore based on an alternative sensor to photomultiplier tubes which does not require a magnetic shielding and ensures compact dimensions. At JET, for instance, CsI(Tl) scintillators are coupled to photodiodes and fit a cylindrical capsule of about 3 cm x 3 cm, diameter x height. Measurements of the gamma-ray emission profile were successfully demonstrated in D plasmas [83]. A drawback of the present setup is its poor energy resolution, which makes it impossible to clearly observe characteristic peaks in the spectrum during a single discharge. This limits the availability of profile measurements to low neutron yield discharges, where the neutron background in the detectors does not dominate over the signal. Another limitation is the slow decay time of CsI(Tl), about 1 μs, which implies a maximum counting rate in the range <100 kHz. Energy band selection is also constrained to 4 intervals only and it can be an issue to clearly distinguish between signal and neutron induced background in some cases.

In order to overcome this limitation, new detectors have recently been developed and make use of silicon photo-multipliers and LaBr$_3$ as an upgrade of CsI(Tl) and photodiodes. The advantages are an energy resolution comparable to that obtained with photomultiplier tubes, i.e. between 4 and 5% at the 662 keV line [135], and a significantly faster pulse width of about 100 ns, which opens up to applications in high neutron yield discharges at MHz counting rates [125]. The use of a dedicated fully digital acquisition system [33], together with the good energy resolution and time response of the new detectors, make it possible to precisely select only the energy bands associated to the specific fast ion reactions of interest, as well as to carefully eliminate the interference of neutron induced events in the spectrum by subtraction of the background in the vicinity of the emission peaks. This is mandatory to allow for measurements of the gamma-ray profile in high performance D and, for the first time, DT plasmas.

2.3 Challenges of the diagnostics and relevance for ITER

The development of suitable collimators is one of the main experimental challenges for neutron and gamma-ray diagnostics. Unlike photons and charged particles, the collimation of neutrons and gamma-rays is less trivial. A careful shielding has to be designed for the actual implementation in a real device. Neutron cameras, for example, practically consist of a block of concrete (say, with a weight of some tons) where conical holes with a length of few meters and a diameter of few cm at the detector position are drilled. The exact dimensions of the concrete shielding are carefully studied by means of lengthy simulations of neutron transport from the plasma to the

detector. Almost always detailed Monte Carlo codes such as MCNP [104] are used. The actual geometry and materials of the tokamak are implemented wth a high degree of fidelity. The aim of the design is to make sure that the fraction of the plasma volume seen by the diagnostic is well defined. For example, in neutron cameras the shielding is studied so that each detector measures the emission as closely as possible only along a chord, as per the diagram in figure 4. No material is a perfect neutron absorber and plasma volumes that are not intended to be seen by the diagnostics also emit neutrons, which can reach the detector. These so-called scattered neutrons, however, have significantly lower energy than 2.5 or 14 MeV, as they are moderated by the amount of material traversed, and can often be discriminated by setting a suitable energy threshold on the detectors. The discrimination capability between direct (uncollided) neutrons and collided neutrons depends on the quality of the shielding design and the stability and response function of the instrument. Most often, besides concrete, high efficiency thermal neutron absorbers (boron or lithium) are included in the design, as well as effective hydrogen rich moderators, for example the widely used polyethylene or, in some cases, water. A side effect of neutron moderation and capture is the production of background gamma-rays. These are born from unavoidable spontaneous nuclear reactions between neutrons and shielding materials or from inelastic neutron scattering. For this reason, a careful simulation of the background gamma-ray generation by neutrons and its transport is also an important task. Gamma-ray absorbers, most popularly lead or iron, are included in the design and generally placed in vicinity of the detector. An additional difficulty comes from the possible further generation of gamma-rays by these absorbers when they are arranged in a neutron field. An iterative approach that proceeds by trial and error is often adopted in the simulations. In case of gamma-ray measurements, specific neutron attenuators must also be placed in front of the detectors to limit the background produced by the interactions of the direct neutrons with the bulk material of the instrument [16, 19, 32]. Here the preferred choices are polyethylene for D plasmas and LiH [22] for DT plasmas.

Practical constraints that limit the design, for both neutron and gamma-ray measurements, are then the weight and the space. Typically, the weight has to be limited to a few tons, which constrains the amount of concrete that can be used. Space is also an issue, as a large number of other diagnostic systems must also be deployed in a tokamak. In practice, only one horizontal and one vertical neutron/gamma-ray camera (see figure 4) with about 20 detectors in total, a few high resolution gamma-ray spectrometers and one D and one DT high resolution neutron spectrometers are possible at most.

From the physics point of view, a difficulty in the interpretation of data is the indirect relation between the fast ions and the spectrum and spatial profile of nuclear radiation. The most common approach is to start from a model of the fast ion distribution function and use it to calculate the expected, spatially resolved spectrum of nuclear emission by dedicated Monte Carlo codes [116, 29], as well as the specific signals seen by each instrument, taking into account the details of its response function (which must be carefully simulated and experimentally validated) and radiation transport from the plasma to the detector, which includes an evaluation of the extent of the background (gamma-rays and scattered neutrons). A comparison between the

synthetic signal and the actual measurement reveals whether the input fast ion model is compatible with the data or must be improved. An alternative is the tomographic inversion of the measured spectra by velocity-space tomography (Section 6). Generally, neutron emission simulations are easier, as there are only two fusion reactions that produce neutrons, i.e. $d(d,n)^3$He and $t(d,n)^4$He . The cross sections are well established. γ-ray emission simulations are more challenging. There is a large number of reactions that lead to gamma-ray emission. This opens up to the simultaneous observation of different fast ions at the same time, rather than only deuterons and tritons as for neutrons. However, this also make the simulation more complex. An additional difficulty comes from the relatively limited availability of good cross section data for a number of reactions. The most simple parameter to simulate is the intensity of the emission, as this solely requires knowledge of the total cross section. Even in this case, however, measurements of the differential cross section at one specific emission angle (termed the excitation function) are sometimes available only and little is known about the full differential cross section, for example its anisotropy as a function of energy (see the discussion of [120]). Besides, some of the emission peaks can depend on the de-excitations of multiple excited states by cascade transitions [172, 131] and knowledge of the differential cross section to populate each of the excited states would be required for a full simulation. A similar argument applies to peak Doppler broadening studies, as the detailed line shape is even more sensitive to the anisotropy of the differential cross section. Presently missing cross section data could be measured at a large number of existing nuclear facilities, once a list of the most important and intense reactions for fast ion diagnostic applications has been compiled based on present experience.

The absolute intensity of the gamma-ray emission depends not only on the cross section and the fast-ion distribution function but also on the impurity concentration which is often not well known. However, the ratio of characteristic peaks from the same reaction as well as the peak Doppler broadening are independent of the impurity concentration and are related to the fast ion distribution function only. In practice, complications arise. For some reactions the Doppler broadening and peak ratio tend to saturate at high fast ion energies (say, at a few hundreds keV tail temperatures for radio-frequency heating scenarios) and the absolute intensity of the emission must be also taken into account to extract quantitative diagnostic information at these energies. Here, a fundamental advantage comes from the fact that the absolute intensity often changes as a power law of the fast ion temperature, with typical exponents significantly larger than one whereas it depends only linearly on the impurity concentration. An uncertainty even up to a factor of 3-4 on the impurity concentration is therefore of little practical relevance to constrain the fast ion distribution function.

If neutron and gamma-ray diagnostics certainly present experimental and interpretation challenges, they are also essential for high power tokamaks, such as JET and even more ITER. The main advantage is the increasing (by orders of magnitude) availability of neutron and gamma-ray fluxes in large, high performance devices, which implies a largely improved signal to background ratio and significantly lower integration time to obtain data at an acceptable statistics compared to most of the present experiments. At ITER, for example, first calculations show that nuclear radiation measurements with a time resolution of relevance to perform fast ion slowing down studies -

or to track fast ion profile changes as a result of MHD instabilities - are within reach. The implementation of nuclear diagnostics at ITER is not entirely different from the present experience at JET. The instruments are placed at some meters from the center of the machine, in some cases behind a bio-shield, where access for system maintenance and detector replacement, albeit seldom, can be envisaged. The extremely harsh plasma conditions of ITER, i.e. an increase of the particle and nuclear heating by orders of magnitude compared to present devices,devices, make the implementation of most fast ion diagnostics extremely challenging, but are of no relevance for neutron and gamma-ray diagnostics. Intrinsic limitations due to the combination of an increased background and significantly smaller cross sections, which plague for example charge exchange based diagnostics as the FIDA in large tokamaks, do not apply. Neutrons and gammas gammas carry information on the very core of a tokamak plasma, including confined fast ions, and are therefore essential to understand plasmas that approach reactor relevant conditions.

3 Neutral Particle Analyzer and Fast Ion D-alpha Spectroscopy

The transfer of electrons from donor neutrals to ions, called charge-exchange, has been detected more than 100 years ago [2] and builds the basis for two important fast-ion diagnostics in fusion devices: neutral particle analyzers (NPAs) and Fast-ion D-alpha (FIDA) spectroscopy. In this section we discuss NPAs and FIDA. NPAs measure the flux of neutralized hydrogen isotopes onto a detector and have a long tradition in fusion research because central ion temperatures could be obtained from the measured energy distribution of neutralized particles during early fusion experiments [1]. These passive measurements were possible because considerable densities of donor neutrals were present in the plasma, due to the low temperatures and low densities. With increasing plasma performance, however, passive charge-exchange measurements are not possible any longer since almost all particles inside the plasma are fully ionized. In contrast, active charge-exchange measurements, based on donor neutrals injected by beams, became possible thanks to the development of neutral beams in the 1970ies [160]. Here, viewing geometries that cross a given neutral beam injection line allow measurements with good spatial resolution. In particular, spectroscopic measurements have become the main diagnostic in many fusion devices to determine the impurity ion temperature, rotation and density [67, 35]. Moreover, active NPA measurements are getting exploited to infer information on the fast-ion distribution function, as well. In addition, the analysis of Doppler shifted charge-exchange radiation of supra thermal particles became possible in recent years due to improvements of the diagnostic equipment (in particular better CCD cameras). In present day experiments, active NPA measurements are getting exploited as well to infer information on the fast-ion distribution function.

   In the following, first the charge exchange process is discussed in section 3.1. Then details on the NPA measurement are given in Section 3.2, followed by a presentation of FIDA spectroscopy in section Section 3.3.
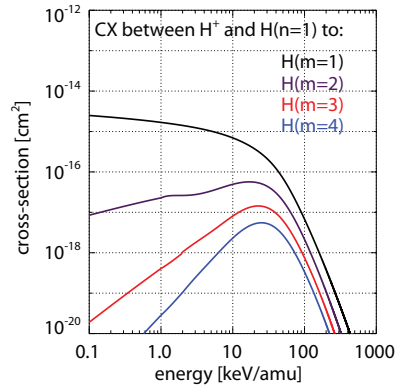
Fig. 9 Charge-exchange cross-sections between hydrogen atoms and hydrogen ions.

3.1 Charge exchange

During charge-exchange, a plasma ion (thermal or energetic) catches the electron from a donor neutral. The momentum exchange is negligible because the electron mass is significantly lower than the ion mass. Thus, the analysis of particles after charge-exchange yields information on the former confined ions. The reaction for hydrogen isotopes can be expressed as:

$$H^+ + H(n) \rightarrow H(m) + H^+ \tag{2}$$
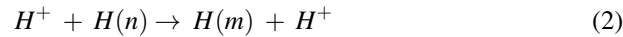
Here, H^+ is the hydrogen isotope ion, $H(n)$ is a hydrogen donor neutral in atomic state n and $H(m)$ is the resulting neutralized ion in atomic state m. The cross section for this process depends strongly on the initial and final atomic states and on the relative collision energy. The cross-sections are plotted in Fig. 9 as a function of the collision energy per atomic mass unit and strongly decrease above about 30 keV/amu (60 keV for Deuterium). This already illustrates that NPA and FIDA measurements are not suitable to detect fast ions in the MeV range.

3.2 NPA

After the charge-exchange reaction, the hydrogen isotopes become neutralized and hence move on straight paths through the plasma. Along their path, the neutral particles might get re-ionized by electron impact ionization, ion-impact ionization or charge-exchange and remain in the plasma. Alternatively, they leave the plasma and hit the walls. This process, called charge-exchange losses, can significantly reduce the plasma energy when large neutral densities are present [53]. These charge-exchange losses can be detected by NPAs which allows the analysis of the fast-ion distribution function.

The technical details of neutral particle analyzers are well described in [99]. In this paper, we focus on the interpretation of the NPA signal. NPA detectors typically have a very good energy resolution and can often resolve isotopes. In addition, the
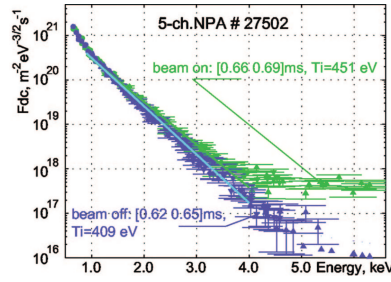
Fig. 10 Exemplaric measurement of the NPA diagnostic at TCV, showing that the signal spans over 6 orders of magnitude. The figure is taken from [77].
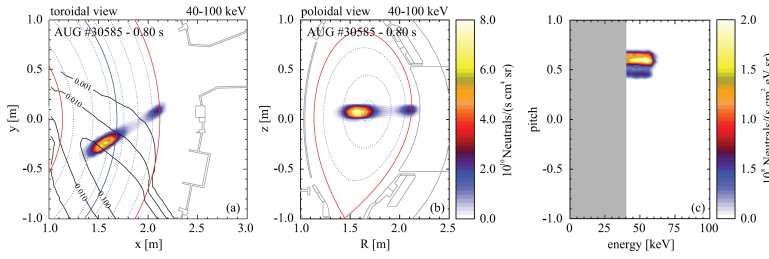

Fig. 11 Toroidal (a) and a poloidal (b) projection of simulated birth locations of neutrals measured with an NPA. The contour lines in (a) illustrate the density of beam neutrals. c) Weight function of the simulated neutral fluxes in the velocity space (pitch, energy). See Section 6 for more details. The figure is taken from reference [152].

signal to noise ratio of the measurement is very good. The latter is mainly limited by the detector characteristics and only to a small degree by additional contributions induced by the plasma. Only neutrons or γ rays might additionally affect the measurement, while e.g. FIDA and CTS measurements are strongly affected by different kinds of plasma radiation such as bremsstrahlung or parametric decay radiation. Thus, already low fluxes of neutralized fast ions provide valuable information. The observed signal can span several orders of magnitude (see Fig. 10). Another highlight of NPA diagnostics is the well defined viewing geometry which defines very well the velocity vector range of the observed particles.

However, NPA measurements are often dominated by passive signals from charge-exchange reactions between plasma ions (fast and thermal) and donor neutrals from the walls. The passive signal contains information on the fast-ion distribution and ion temperature but is difficult to interpret: The density profile of donor neutrals from the walls is typically not well known, which makes the determination of the neutralization position of the detected neutrals challenging. This limits not only the spatial resolution of the measurement but also the velocity space resolution, since the pitch value of fast ions depends on the direction of the local magnetic field. At the plasma edge, for example, the angle between the observation line and the magnetic field is typically different compared to the one in the plasma center (given that the viewing line is not perfectly radial). As an example, Fig. 11 shows a simulation of the birth location of detected neutrals together with the corresponding pitch values. The
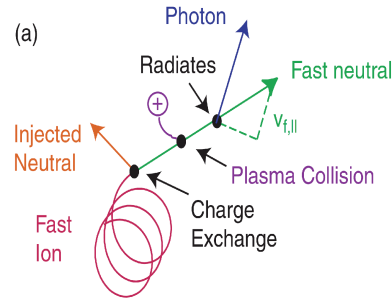
Fig. 12 Sketch of the FIDA emission process. The figure is taken from reference [59].

simulation shows a clear contribution from the plasma edge due to passive charge-exchange as well as an active contribution from the plasma center. The pitch values of the active and passive contributions differ (about 0.65 for the active contribution and about 0.5 for the passive one).

For a quantitative interpretation of NPA measurements, forward modeling is needed. Here, several codes exist such as FIDASIM [61] or DOUBLE [85]. These codes need the background density of neutrals from the walls and a given fast-ion distribution function as inputs. The codes determine the probability for charge-exchange between a given donor neutral and the fast or thermal particle and then follow the neutralized particles though the plasma. The re-ionization along the straight path through the plasma is also accounted for. Accounting for the aperture of the diagnostic and the size of the detector, NPA fluxes can be calculated in absolute units and the corresponding energies and pitch values can be analyzed.

In contrast to passive NPA measurements, active NPA measurements with a modulated neutral beam allow well localized measurements by subtracting the passive fluxes measured when the beam is off. This allows highly sensitive and well localized measurements at one give pitch value. Thus, one obtains information about fast-ions at a specific pitch, R and z location with good resolution in energy. Different parts of the fast-ion phase space can only be addressed by installing several detectors. Such multi detector NPA system are, however, not routinely employed because of the detector size and the limited access to most fusion devices. New developments, such as an in-vessel scintillator based NPA, might provide a better coverage of the phase space in future experiments.

3.3 FIDA

In contrast to the limited access to the phase space of NPA detectors, FIDA spectroscopy covers the whole fast-ion velocity space. However, it exhibits relatively poor resolution in velocity space and can, thus, be seen as a complementary diagnostic to NPAs. FIDA spectroscopy is based on the analysis of the Doppler shifted Balmer alpha emission (n=3 to n=2 at 656.1 nm), emitted by the neutralized particles after charge-exchange (see sketch plotted in Fig. 12). As can be seen in the cross sections plotted in Fig. 9, the charge-exchange cross section from n=1 into the n=3 state is
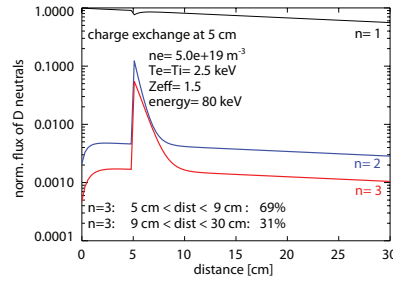
Fig. 13 Population of the quantum states of a Deuterium neutral with 80 keV that undergoes charge exchange after 5 cm with an 80 keV ion with a relative collision energy of 30 keV. From that position on the population of states of the neutralized ion is displayed.

maximum 20 times smaller than the corresponding cross-section into the n=1 state. Thus, about 5% of the fast neutrals are in the n=3 state after charge-exchange reactions. These 5% are much larger than the typical equilibrium fraction of n=3 neutrals. Hence, an overpopulation of the n=3 state is present after the charge-exchange process, which provides strong localized Balmer-α emission within the first few cms after neutralization.

Figure 13 illustrates that the population of the ground state (n=1) of a deuterium neutral is typically three orders of magnitude larger than the n=3 state, assuming typical plasma parameters as given in Fig. 13. At 5 cm, we considered a charge-exchange process with a 80 keV ion and a relative collision energy of 30 keV. From that position on, we continue to plot the state distribution of the neutralized 80 keV ion. Clearly, the n=3 state is overpopulated after charge-exchange and then decays through the spontaneous emission of photons. As indicated, 69% of the FIDA emission is emitted within the first four centimeters after charge-exchange, providing good spatial localization.

The required diagnostic equipment to detect the Doppler shifted Balmer alpha light is basically the same as required for charge-exchange recombination spectroscopy (CXRS), used to infer ion temperature, rotation and density measurements of impurity ions. Lenses collect radiation from the plasma in the visible range and fibers guide this light to a spectrometer that is typically located distant from the fusion device. The distance to the device avoids interference by the magnetic fields or neutrons that can have an effect on the camera attached to the spectrometer. Given that the spectrometer can reach 656 nm (the Balmer alpha line) with a spectral range that is wide enough, every CXRS diagnostic can be used for FIDA measurements. However, for a dedicated diagnostic several optimization criteria should be considered: the signal level of FIDA light is low compared with normal charge-exchange measurements. It is thus important to guarantee enough photons to be detectable by the camera such that the FIDA signal level is well above the read-out noise level. Dedicated FIDA spectrometers are therefore operated using relatively wide entrance slits. This enhances the photon throughput but also increases the instrumental broadening function, i.e. reduces the wavelength resolution. Moreover, measuring the whole D-alpha spectrum with good signal to noise ratio is hardly possible with a standard CXRS spectrometer because the edge D-alpha emission is very bright and would cause satu-
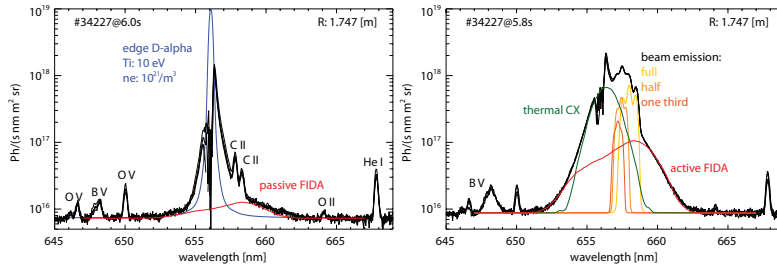
Fig. 14 Active and passive FIDA spectrum measured at ASDEX Upgrade together with predictions from FIDASIM.

ration effects of the camera. Standard CXRS diagnostics used for FIDA are therefore limited to measure either blue or red-shifted FIDA light by keeping the un-shifted edge-radiation away from the detector chip. More advanced FIDA systems, as used at DIII-D [108], ASDEX Upgrade [50], MAST [102], NSTX [13], EAST [65] and LHD [128] typically block the edge-D-alpha radiation from the plasma edge by using additional lenses and a wire in the intermediate image.

A passive FIDA spectrum and an active FIDA spectrum, measured at ASDEX Upgrade are potted in Fig. 14a and Fig. 14b on a semi-logarithmic scale. The radiation around 656 nm is blocked by a wire in the spectrometer setup. The passive spectrum consists of bremsstrahlung and line radiation mainly emitted close to the plasma edge. As already mentioned, the Balmer-α radiation from the plasma edge is particularly intense and dominates the spectrum. In blue we depict a synthetic edge Balmer-α line with a realistic intensity. The line is broadened by the Doppler effect (here we assume 10 eV) and by Stark broadening which appears in plasma regions where the electron density is large (here we consider an electron density of $10^{20}/m^3$). In addition, impurity lines are present, of which Carbon and Oxygen lines have been identified in the plot. Finally, passive FIDA radiation can be observed which is present due to charge-exchange reaction between fast ions and neutrals from the walls. In figure 14a, simulated passive FIDA radiation from FIDASIM is plotted in red assuming a neutral density profile from TRANSP/FRANTIC. In particular when there is a clear overlap between the fast-ion density and the profile of neutrals (strongly decaying towards the center) e.g. during off-axis NBI, this type of FIDA radiation can be observed. Due to the missing spatial localization of passive FIDA light, the interpretation is difficult. Thus, passive FIDA is typically avoided or removed from the spectrum by studying the active signal using modulation of the neutral beam, whose path is crossed by the lines of sight.

A spectrum with additional active contributions is plotted in Fig. 14b, together with the simulation from FIDASIM. The simulation consists of charge-exchange radiation emitted by neutralized thermal ions (thermal cx, green) and by neutralized fast ions (red), as well as by impurity ions. In addition, the beam emission is present in active spectra, which is the direct radiation from fast neutrals injected by neutral beams. The beam emission consists for positive NBI sources of the full, half and one third energy components, which are each split by the motional Stark effect. When selecting lines of sight for FIDA spectroscopy, it is essential that the beam emission
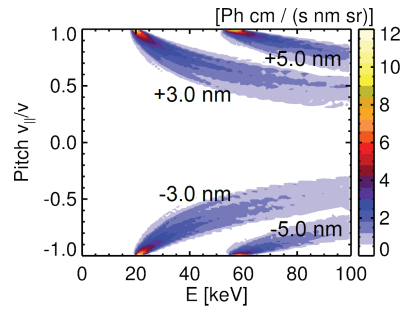
Fig. 15 Weight functions for one toroidal viewing line of the ASDEX Upgrade FIDA system and for different wavelength shifts. The figure is taken from the reference [178].

does not exhibit too strong Doppler shifts. Viewing lines close to perpendicular to the NBI path are beneficial. Otherwise, the FIDA radiation is superimposed by the beam emission and can hardly be analyzed.

The Doppler shift of the FIDA radiation contains information on the fast-ion velocity space distribution. In general, a given Doppler shift can be related to a minimum energy that the ion must have to produce this Doppler shift. The larger the Doppler shift, the larger this minimum energy is. However, an upper limit for the ion energy for a given Doppler shift cannot be given. Low Doppler shifts can be produced due to highly energetic ions if these move close to perpendicular to the viewing geometry. This can be seen by the nature of the Doppler effect:

$$\lambda_D - \lambda_0 = u\lambda_0/c \qquad (3)$$

Here, c is the speed of light in and λ_0 is the unshifted D-alpha wavelength (656.1 nm), u is the projected velocity of the ion on the line-of-sight.

To describe the observed fast-ion velocity space region when analyzing a given Doppler shift with a given viewing geometry, weight functions are used [57,143], see Section 6. The weight functions can e.g. be calculated by FIDASIM and yield the expected FIDA photon flux when first multiplying a given weight function with a fast-ion distribution function and after integration in the fast-ion velocity space. Fig. 15 shows weight functions for a tangential viewing geometry and different wavelengths. Clearly different parts of the fast-ion velocity space can be analyzed when looking at different wavelength shifts.

If all Doppler shifts were accessible, information on the whole fast-ion velocity space distribution would be obtained from a single line of sight [141]. However, in particular at low wavelength shifts, the FIDA radiation is superimposed by the beam emission, thermal charge-exchange emission and the cold edge D-alpha line. Thus, a given viewing geometry can only probe a certain part of the fast-ion velocity distribution. Different viewing geometries are needed to obtain a full coverage. An example is the 5 view FIDA system at ASDEX Upgrade [178], plotted in Fig. 16a. In Fig. 16b, the corresponding weight functions for blue and red-shifted wavelength ranges are given. This FIDA system with five different viewing direction was designed to allow studies of the fast ion velocity distribution function by velocity-space tomography.
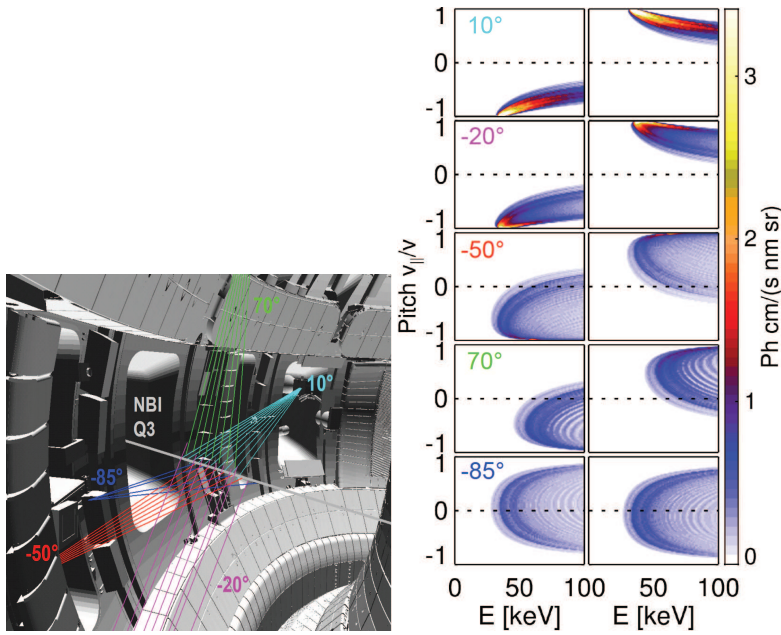
Fig. 16 a) Geometrical arrangement of the line of sight arrays at ASDEX Upgrade [178]; b) Weight functions corresponding to the different viewing geometries and two different wavelength ranges [178].

Examples of measured fast-ion velocity distribution function are presented in Section 6.

The active FIDA radiation is localized along a neutral beam. By using radially distributed lines of sight, radial profiles with information on fast ions can be observed. In particular when using viewing lines that are tangential to the magnetic field lines at the intersection with a given NBI path, good spatial resolution can be obtained. To generate radial profiles, each spectrum needs to be integrated within a given wavelength range and the passive contribution needs to be subtracted. Here, either frames without NBI are subtracted or a flat line describing bremsstrahlung and measured elsewhere in the spectrum (e.g. 664-667 nm) is subtracted.

For the quantitative analysis, the measured profiles can be compared with radial profiles from FIDASIM. Here, it should be noted that an absolute calibration of CXRS diagnostics is demanding. Cameras might degrade or vacuum windows might get coated with layers, such that an initially good calibration is not trustworthy. In the case of FIDA spectroscopy, it is therefore recommended to cross check the intensity calibration by additionally analyzing the beam emission and the level of bremsstrahlung. Both additional spectral components are simulated by FIDASIM and can be compared with the measurement. Only if this check is successful, reliable conclusions based on the FIDA data can be made. Another approach is to analyze the ratio of the FIDA signal to the beam emission intensity (BES). Since FIDASIM simulates both contributions, the comparison of the measured FIDA/BES signal with the
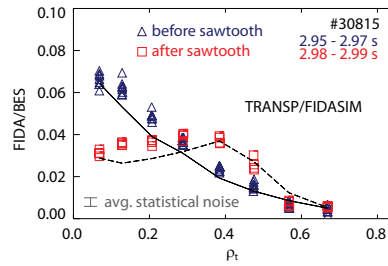
Fig. 17 Radial FIDA/BES profiles measured before and after a sawtooth crash in ASDEX Upgrade. The measurement is compared with synthetic profiles from FIDASIM, based on predicted fast-ion distribution functions from TRANSP [51].

simulated one is independent of an intensity calibration. An example of a measured FIDA/BES signal from ASDEX Upgrade is plotted in Fig. 17.

The analysis of highly energetic fast ions with FIDA spectroscopy is difficult. The most important charge-exchange cross section for FIDA is the one from n=1 to n=3 because it directly populates the atomic state, responsible for the Balmer-α emission. This cross-sections peaks at the relative collision energy of about 30 keV/amu. At higher collision energies, such as 200 keV/amu, the cross section is lower by more than two orders of magnitude lower. In addition, the FIDA emission from highly energetic ions can spread over a large wavelength range due to the gyro-motion and the Doppler effect. Thus, the expected FIDA intensity per wavelength bin reduces significantly with increasing energy.

At low signal levels, the measurement becomes affected by the background noise. This background noise consist of hardware related noise such as the cameras read-out noise. In addition, it consists of photon noise, which follows the Poisson statistic ($\sigma = \sqrt{N_{photons}}$). While readout noise can be almost eliminated by long exposure times or the application of an electromagnetic (EM) gain in modern CCD cameras, the level of photon noise is difficult to reduce. In particular the presence of bremsstrahlung limits the analysis of FIDA radiation because this radiation is present in FIDA spectra as a flat offset. In cases where the square root of the number of photons from bremsstrahlung exceeds the number of photons from the FIDA process, the noise level is larger than the actual measurement. Thus FIDA spectroscopy is not possible any longer since it is not possible to discriminate between noise and FIDA radiation. This is typically the case in plasmas with high electron densities where the level of bremsstrahlung is high and where the neutral beam attenuation is strong, reducing the number of donor neutrals. A clear condition, up to which density FIDA measurement are possible cannot be provided because this additionally depends on the fast-ion, impurity concentrations, and NBI power and energy an on the FIDA diagnostic. By e.g. using a spectrometer with more photon throughput or using longer exposure times the signal to noise ratio can be improved. However, increasing the flux of photons by a factor x does only improve the signal to noise ratio by $\sqrt{(x)}$, well explained by the photon noise. With respect to ITER, one can therefore already state that core localized FIDA measurements will be very challenging. High electron densities, low fast D-ion densities and low donor densities due the to high energy

beams (the higher the energy, the less particles are injected at a given power) will result in weak FIDA signal strengths. In combination with the expected high levels of bremsstrahlung, the FIDA signal is likely obscured by photon noise.

By increasing the photon throughput of the spectrometer or using longer exposure times the situation can be improved a bit, since photon noise scales with $\sqrt{N_{photons}}$. A clear condition, up to which density FIDA measurement are possible cannot be provided because this additionally depends on the fast-ion, impurity concentration and NBI power and energy. With respect to ITER, one can, however already state that core localized FIDA measurements will be very challenging. High electron densities, low fast D-ion densities and low donor densities due the to high energy beams (the higher the energy, the less particles are injected at a given power) will result in weak FIDA signal strengths. In combination with the expected high levels of Bremsstrahlung, the FIDA signal is likely obscured by photon noise.

4 Collective Thomson Scattering

The Collective Thomson Scattering (CTS) diagnostic is not as wide-spread as FIDA, NES, or GRS. However, it plays an increasingly important role in fast ion research and can often be installed comparatively easily in devices with ECRH systems. CTS is a passive diagnostic with good temporal and spatial resolution. CTS diagnostic based on a far-infrared laser for ion temperature measurements was initially used at the TCA tokamak [4]. Later the CTS diagnostics at TFTR [181, 97], JET [8, 9], TEX-TOR [11, 103], ASDEX Upgrade [101, 100], LHD [115, 114, 93], W7-AS [170], and FTU [127] used microwaves as a source of probing radiation for the fast ion CTS. The diagnostic is also used for measurements of the ion temperature [166, 168], isotope ratio [92, 162, 166, 163, 164], and plasma rotation[168, 169]. In inertial confinement fusion experiments, laser-based CTS is regularly used for ion temperature measurements [54, 137]. Here we concentrate on microwave-based design of the diagnostic.

4.1 Physics principles

The injected electromagnetic radiation accelerates the charged particles in the plasma which in turn radiate which is referred to as scattering. As the ions are much more massive than electrons, scattering off electrons dominates scattering off ions by orders of magnitude. The scattering off electrons bears signatures of microscopic fluctuations in the plasma. Of particular interest for fast-ion CTS are the fluctuations induced by fast ions. The acceptance cone of the antenna and the probe beam intersect in the so-called overlap volume which defines the measurement location in the plasma. Fig. 18 depicts the geometry of CTS: $\mathbf{k^i}$ is the wave vector of incident (probing) radiation, $\mathbf{k^s}$ is the wave vector of the received scattered radiation, and $\mathbf{k}^\delta$ defines the direction along which the fluctuations are resolved:

$$\mathbf{k}^\delta = \mathbf{k^s} - \mathbf{k^i}, \qquad (4)$$

If the Salpeter parameter $\alpha = 1/(k^\delta \lambda_D) > 1$ [150], the scattering is received from collective fluctuations in the plasma, i.e. those induced by ion motion and MHD activity.

Here k^δ is the magnitude of $\mathbf{k}^\delta$ and λ_D is the Debye length. An angular frequency shift in the scattering radiation:

$$\omega^\delta = \omega^s - \omega^i, \tag{5}$$

can be approximately related to an ion velocity, $\mathbf{v_{ion}}$, by

$$\omega^\delta \approx \mathbf{v_{ion}} \cdot \mathbf{k}^\delta = u k^\delta. \tag{6}$$

Here ω^s and ω^i are the angular frequencies of the scattered and incident radiation and u is the projection of the ion velocity on the direction of $\mathbf{k}^\delta$.

The spectral power density of received scattering radiation is described by the equation of transfer

$$\frac{\partial P^s}{\partial \nu} = P^i O_b \omega^i \omega^s r_e^2 n_e \frac{G S(k^\delta, \omega^\delta)}{2\pi c^2}, \tag{7}$$

where P^i is the probing power; O_b is the so-called overlap integral which represents a measure of intersection between the probing and the receiving beams [7]; ω^i and ω^s are the angular frequencies of the incident and scattering waves; r_e is a classical electron radius, n_e the electron density, c is the speed of light in vacuum, G is the so-called geometrical form factor which quantifies the efficiency of scattering from the probing beam to the scattering beam [66]; S is the so-called scattering function which defines the shape of the scattering spectrum as a function of plasma parameters, in particular the projection of the fast-ion velocity distribution function. The scattering function $S(k^\delta, \omega^\delta)$ is derived in several approximations, electrostatic [66] and fully electromagnetic [7]. The scattering function depends on the projection of the fast ion velocity distribution function on the $\mathbf{k}^\delta$ direction:

$$g(u) = \iiint_{R^3} f(\mathbf{v}) \delta \left(u - \frac{\mathbf{k}^\delta \cdot \mathbf{v}}{k^\delta} \right) dv_{||} dv_\perp^1 dv_\perp^2 \tag{8}$$

This 1D projected fast-ion velocity distribution function depends strongly on the angle, ϕ, between $\mathbf{k}^d elta$ and the local magnetic field vector in analogy to FIDA.

4.2 Experimental Setup

The CTS diagnostic consists of two main parts: one part provides the probing radiation and the other part detects the scattered radiation. Typically, gyrotrons are used as sources of the probing radiation: using microwaves allows much flexibility in the choice of the geometry with a Salpeter greater than one. For shorter wavelength only forward scattering geometries ensure the collective scattering regime. Infrared lasers with a wavelength of 10.6μm have also been used as probing sources, but the scattering angle had to be very small, less than $1°$ in order to satisfy the Salpeter criterion. The CTS diagnostics based on infrared lasers worked on the ATF torsatron [134] and the JT-60U tokamak [94, 88, 89]. A feasibility study of using infrared-laser based CTS for ITER was done [10], but it was found that 60 GHz microwave CTS has the best performance.
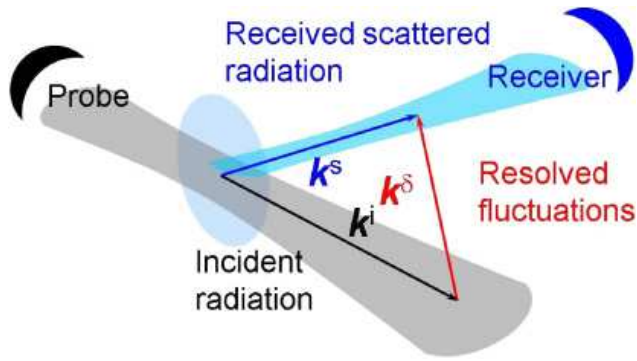
Fig. 18 Geometry of Thomson scattering: $\mathbf{k^i}$ is the wave vector of incident (probing) radiation, $\mathbf{k^s}$ is the wave vector of the received scattering radiation, and $\mathbf{k}^\delta$ is the wave vector of resolved fluctuations. The figure is taken from [106]
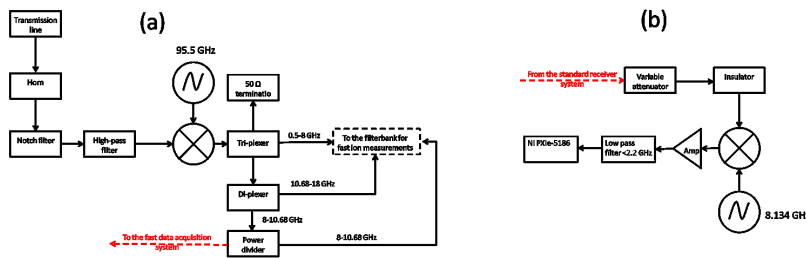

Fig. 19 A schematic of the CTS receiver at ASDEX Upgrade. The left panel (a) depicts all parts of the receiver from the horn to the filter bank and an additional mixing stage with the fast data acquisition is shown on the right panel (b). More detailed description is available in reference [167].

Microwave-based CTS for fast ion studies has been successfully operated on TEXTOR [11, 110, 106, 111, 109, 12, 91], ASDEX Upgrade [139, 112, 101, 100, 132, 133, 74], LHD[115, 114, 93], Wendelstein-7AS [170, 153], and FTU [127]. TEXTOR and Wendelstein 7-AS are now out-of-service.

In CTS diagnostics, the probing radiation and the scattered radiation travel through transmission lines. The transmission lines often include steerable mirrors in order to provide with the geometrical flexibility, polarizers (in some implementations of the diagnostics polarizers are incorporated into the receiver [96]), and a matching optics unit which is a coupling device between the transmission line and the source of probing radiation or the microwave receiver. The transmission line can be quasioptical, as at TEXTOR [109] or Wendelstein 7-X [27], or made of oversized waveguides as on ASDEX Upgrade [37], LHD [156], Wendelstein 7-AS [170], FTU [127], and is being designed for ITER [90]. Often CTS shares the transmission lines with the ECRH system, as at ASDEX Upgrade, LHD and Wendelstein 7-AS, which means that two transmission lines are not available for ECRH during CTS measurements. ITER will have dedicated microwave transmission lines for the CTS diagnostic.

CTS receivers are heterodyne radiometers. A schematic of the receiver at ASDEX Upgrade is shown in Fig. 19, left panel. The CTS diagnostic does not only receive

the scattered radiation but any other microwave radiation in the detection frequency range. These are ideally electron cyclotron emission (ECE) and stray radiation from the gyrotron. The scattering power is typically 11-12 orders of magnitude smaller than the probe power and typically is in the μW range. The exact quantity is determined by the beam overlap integral, the electron density, the scattering function, and the geometrical form factor [6]. The probe power is usually in the range of several hundred kW. 1 MW is foreseen for CTS at ITER. If even a tiny fraction of the injected radiation entered the receiver as stray radiation, several components in the receiver may be damaged. Therefore the receiver must be protected by a notch filter (or a cascade of notch filters). The depth of the notch is around -100 dB [36] in the stopband of 200-300 MHz width. The insertion loss is about -2dB per notch filter. Additionally to the notch filters, the RF part of the receiver is protected by a variable voltage-controlled attenuator (VCVA) with maximum attenuation of -40 dB. The VCVA is needed in order to protect the receiver at the moments when the probe is switched on or off. At these times the gyrotron frequency drifts and may potentially drift outside the stopband of the notch filter, which may cause the receiver damage or cause gain compression of the intermediate frequency amplifiers.

Another necessary component of the CTS receiver is a band-pass filter. The band-pass filter ensures that the RF signal in the desired frequency range is transmitted further for down-mixing, thus avoiding aliasing effects. Some CTS receivers, for example the CTS receiver at ASDEX Upgrade designed for operation with a 105 GHz source are additionally equipped with a low-pass filter in order to protect the receiver from higher frequency stray radiation of the ECRH gyrotrons [37]. An insulator before the mixer is needed for the suppression of back reflections from the mixer.

The RF signal is typically mixed down so that the resulting frequency of the signal is in the range of 10-20 GHz. This frequency range is comfortable to work with as there is a large variety of affordable low-noise microwave components. After amplification, the intermediate frequency signal comes to a triplexer as on TEXTOR [161]] or a 4-way power splitter (a combination of a triplexer with a diplexer) as on ASDEX Upgrade [167]. At ASDEX Upgrade, only three outputs are used and the fourth is used only for auxiliary purposes. The power splitting is done as the amplitude of the spectral power density of the scattered radiation strongly depends on the frequency, such that it is advantageous to use different amplifications for various frequency ranges. Another reason is to avoid the non-linear effects of the amplifiers on the spectrum, when not only the signal at its own frequency is amplified but the harmonics of it as well. In the vicinity of the probing frequency the scattering spectrum is dominated by the contributions from thermal particles and has large spectral power density, often comparable with the spectral power density of the ECE background. This part of the spectrum needs the least amount of amplification. The wings of the frequency spectrum of the scattering radiation are dominated by energetic particles. The spectral power density of the scattering signal is typically two orders of magnitude lower and thus the signal requires stronger amplification. After amplification, the signal is fed to a filter bank which has 30-50 channels. As an example, the frequency response of intermediate frequency filters in the filter bank of the 77 GHz CTS diagnostic on LHD is displayed in Fig. 20. For the frequency channels near probing frequency the bandpass filters have 3 dB width of 100 MHz. The frequency
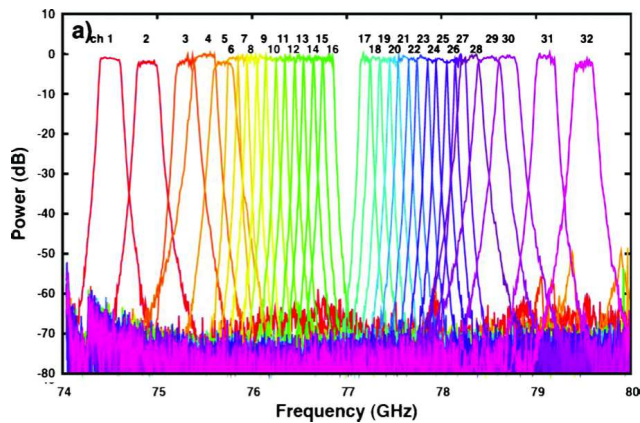
Fig. 20 Characteristics of band-pass filters in the filter bank of the CTS diagnostic at LHD [93].

channels in the filterbank monitoring frequencies with large frequency shifts usually have larger width because the signal in these fast-ion channels is much lower.

At the moment fast acquisition systems with a bandwidth of several GHz and respective sampling rate are becoming a common in CTS [161, 167, 115, 114]. For the use of fast acquisition cards, a fraction of the intermediate frequency signal is taken from one of the outputs of a power divider or triplexer, amplified, and mixed down once again to the frequencies of 1-10 GHz where it can be sampled by the fast ADC. In order to obtain the frequency spectrum, the sampled signal is Fourier transformed. An example of the receiver which features the fast acquisition system is shown in Fig. 19. A key feature of receivers with the fast data acquisition is a very high frequency resolution which is defined by the length of the Fourier window. A frequency resolution of about 1 MHz is easily achievable. This allows the detection of spikes in the spectra that are not easily seen using filterbank-based detection. Such an extension to the CTS receiver is typically used for the bulk ion measurements which require high frequency resolution. In any case, such systems allow a measurement of the gyrotron frequency despite the depth of the notch filters so that any drift in the gyrotron frequency can be tracked and accounted for in the data analysis. This technique could also be used for fast-ion measurements but this has not yet been done.

4.3 Operational regimes

CTS is a flexible instrument, and this operational flexibility can be exploited to improve the signal-to-noise ratio of the measurements. In the following section we discuss the main control parameters of the diagnostic.

Beam overlap It is assumed in the CTS model that the received scattering radiation originates from the region where the probing and receiving beams overlap. Quantitatively it is described in the equation of transfer (equation (7)). The location of the

overlap volume and the beam overlap O_b are calculated using beam tracing or ray tracing codes like TRAVIS [98]. However, the electron temperature and density profiles are not known precisely and microwaves can be strongly refracted. If the beam width is narrow or the location of the overlap volume is far from the launching and receiving mirrors, the location of the beam overlap volume may significantly differ from theoretical estimations. A scenario with a long distance between the measurement volume and the receiver mirrors and enhanced refraction occurs typically in measurements of ions with pitches close to ± 1. In such scenarios, the calculated mirror positions for the best possible overlap at a given location may serve only as an initial guess. The real mirror settings for the maximum overlap O_b from the equation of transfer (7) are found during the so-called overlap sweep. During the sweep, the probing beam is fixed and the receiver beam is scanned across the probe. The scan is performed around the position of the theoretically defined overlap. The procedure is described in detail in references [109, 106] and illustrated in Fig. 21. The sweep serves the purpose of finding the best beam overlap, and methodologically it also establishes that the measurements are local.

Background subtraction The CTS receiver receives microwaves in the predefined frequency range and polarization. Therefore, the scattered radiation is measured together with any other radiation referred to as background radiation. A prime source of the background is electron cyclotron emission for the microwave CTS. For the infrared laser CTS the sources of the background are thermal radiation of the first wall surface and atomic emission lines. In order to subtract the background, the power of the probing beam is modulated. Then the measured spectral power density of the scattering signal is

$$\frac{\partial P^s}{\partial \nu} = \left.\frac{\partial P}{\partial \nu}\right|_{on} - \left.\frac{\partial P}{\partial \nu}\right|_{off}, \tag{9}$$

where $\frac{\partial P^s}{\partial \nu}$ is the spectral power density of the scattering radiation, $\left.\frac{\partial P}{\partial \nu}\right|_{on}$ and $\left.\frac{\partial P}{\partial \nu}\right|_{off}$ are the measured spectral power densities with the gyrotron switch on or off, respectively. The modulation of the gyrotron is displayed in Fig. 21. The time resolution is limited to about 4ms with this technique, corresponding to 2ms on and 2ms off, as this is currently close to the modulation frequency limit for gyrotrons. However, the gyrotron power can be modulated about 10 times faster, for example between 90% and 10% of the full power. The better time resolution is sometimes highly advantageous if the signal varies on the millisecond time scale. With this technique, the background radiation cannot be subtracted, since there is still a small scattering component, but the difference in signal levels still allows the inference of the parameters of interest. One may also occasionally switch the gyrotron off in this scheme to get a measurement of the background.

The spectral power density of the ECE background is decisive for the signal-to-noise ratio (SNR) of the diagnostic [6]:

$$SNR = \frac{\partial P^s}{\partial \nu} \sqrt{\frac{WT}{2\left(\frac{\partial P^s}{\partial \nu} + \left.\frac{\partial P}{\partial \nu}\right|_{off}\right)^2 + 2\left(\left.\frac{\partial P^b}{\partial \nu}\right|_{off}\right)^2}}, \tag{10}$$
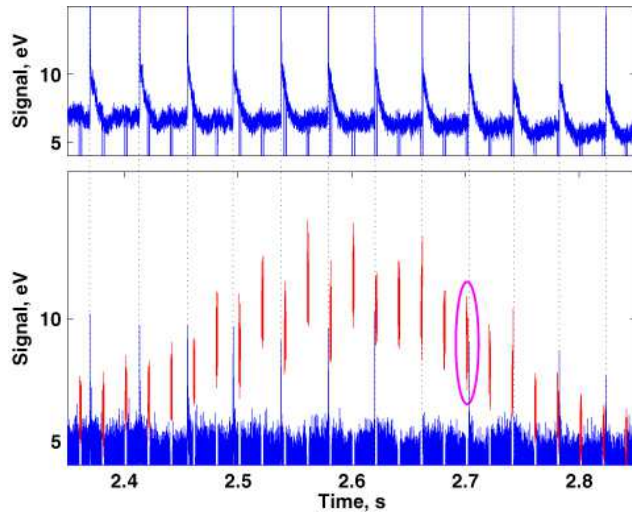
Fig. 21 The source modulation in the CTS experiment at TEXTOR during the so-called overlap sweep in shot 111506, when the receiver beam is swept across the probing beam. The upper and lower panels depict the time traces of channels 42 and 37, respectively. Channel 42 receives no scattering radiation, only the ECE background. Therefore, neither the overlap sweep nor the power modulation of the probe are visible. Channel 37 receives the fast ion scattering signal and, when the overlap between the receiver and probing beams is significant, the scattering signal emerges as a difference between the received power in the gyrotron-on (red) and gyrotron-off (blue) phases [106].

where W is the bandwidth of the frequency channel, T is integration time, and $\frac{\partial P^b}{\partial v}\big|_{off}$ is the spectral power density of the background signal.

The amount of the background radiation strongly depends on the presence of the ECE resonances in the plasma at the receiving frequencies, polarization of the receiver, plasma parameters, etc. In fast ion CTS the frequency is chosen in a way that the waves do not meet a cut-off or absorption/emission layer at positions with significant electron densities before the measurement volume. A sketch illustrating the dependence of the amount of ECE seen by a receiver as a function of the probing frequency is shown in Fig. 22. At the moment a 300 GHz gyrotron is development for CTS at LHD, which would allow operation at the frequencies above the third harmonic of ECE with very small spectral power density of the background radiation [182]. The spectral power density of the scattering signal depends on the input power and on the scattering channel, X to X, O to O, X to O and O to X where X and O refer to the extraordinary and the ordinary modes, respectively. This dependency is described in the geometrical form factor from equation (7). The integration time should be chosen so that the plasma parameters such as temperature, density and fast ion content do not change significantly during the averaging period.

Sometimes the spectral power density in the gyrotron-on period is larger than that in the gyrotron-off period even if the probe and receiver beams do not overlap. Such kind of spurious signal can be subtracted by using a second receiver not intersecting the probe beam which is referred to as a passive view. A second receiver for the back-
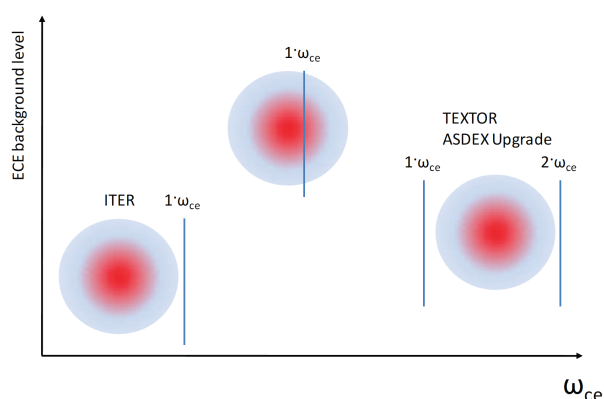
Fig. 22 The sketch qualitatively demonstrates the amount of the ECE background seen by the receiver from the position of ECE resonances in plasma at the detected frequencies. The cases of the fast ion CTS at ASDEX Upgrade, TEXTOR, and future CTS at ITER are shown [105]. Sometimes resonances in the plasma after the measurement volume can be advantageous as they absorb part of the microwaves.

ground subtraction is currently installed on ASDEX Upgrade [112] and is planned for the 154 GHz CTS diagnostic at LHD. It allows to solve the problem with the spurious signal in the measured spectrum and to achieve quantitative agreement between the measured and simulated fast ion velocity distribution functions in the discharges with the CTS spectra that are contaminated by the spurious signal. An installation of the double receiver CTS diagnostic is shown in Fig. 23. Ideally, the active and the passive views should measure the same background when the gyrotron is off. This technique works best for receiver beams that are perpendicular to the magnetic field, such that refraction is small and the two beams are toroidally displaced but otherwise similar. Sometimes spurious signal can also be mitigated by the fast modulation technique described above.

4.4 Energetic Ion Measurements by CTS

The diagnostic is capable of resolving fast ion dynamics on the time scales which are limited by SNR or the gyrotron modulation frequency. Fast-ion redistribution due to the sawtooth oscillations has been measured by CTS [110].Later those findings were confirmed by other fast ion diagonstics. Qualitative [109, 139] and quantitative agreement [112, 106, 132] between the measurements and the Monte-Carlo simulations is achieved. Fig. 24 demonstrates quantitative (panels (a) and (b)) and qualitative (panels (c) and (d)) agreement between the CTS measurements in TEXTOR and Monte-Carlo simulations by ASCOT and VENUS codes. The quantitative agreement between the measurements and the simulations is achieved in the plasma center.

The CTS diagnostic is sensitive to a variety of MHD effects, since the probing radiation scatters off fluctuations of density, magnetic field, and electric field. Fast ions are a source of free energy for a number of instabilities, such as fishbone instability, lower hybrid instability, Alfvén eigenmodes, ion cyclotron emission, etc. Some
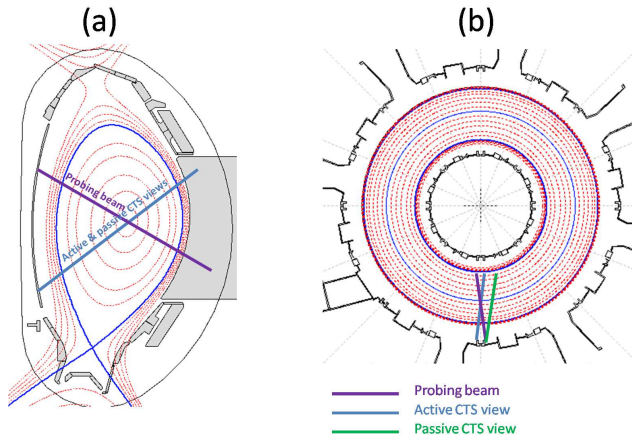
Fig. 23 The double receiver CTS setup at ASDEX Upgrade that allows the subtraction of overlap-independent spurious signal in the received scattering spectra. The passive CTS view does not intersect the probing beam. On the left panel (a), the poloidal cross-section of ASDEX Upgrade is shown together with the probing beam (magenta), active and passive CTS receiver views (blue). The active and passive views have the same projection in this plane. On the right panel (b) the toroidal cross-section of the setup is shown. The active and passive CTS receiver views are shown in blue and green, respectively.
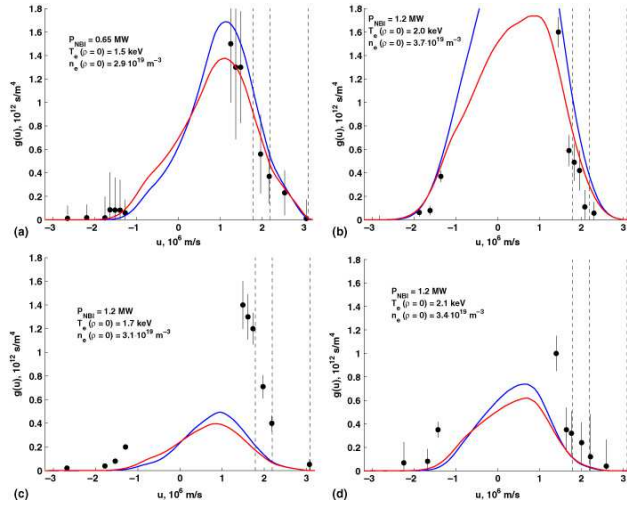

Fig. 24 Projections of the the fast ion velocity distribution function in TEXTOR at different radial positions and projection angle to the magnetic field. The black dots correspond to the measured values of the projection of the fast ion velocity distribution function, red and blue lines correspond to Monte-Carlo simulations with ASCOT and VENUS. Panels (a) and (b) demonstrate the results close to the plasma center; (c) and (d) are the results of the off-axis measurements. The figure is taken from [106].

of these instabilities have a distinct footprint in the CTS spectrum and can therefore serve as a qualitative indicator of the presence of energetic ions [153, 107].

4.5 Prospects for ITER

A feasibility study [10] found that CTS is capable of measuring fusion-born α-particles in ITER both with the radial resolution of $\approx$20-50 cm and with temporal resolution of about 100 ms. 1 MW gyrotron operating at 60 GHz will be used as a source of probing radiation. The parts of the phase space which give rise to the CTS signal have been identified [140] and the effect of the auxiliary heating on the fast ion signal has been investigated [138]. Currently the diagnostic is being designed with seven lines of sight [90, 95] and will be located in the port-plug in the equatorial port 12. A full drawer will be allocated to the CTS diagnostic at ITER. A feasibility study of isotope ratio measurements using CTS at ITER have been conducted [165] and conclusively demonstrated that the proposed CTS system with some minor adjustments is capable of such measurements, but until now ITER CTS is dedicated to measurements of α particles and other fast ions.

5 Fast Ion Loss Detector

In contrast to the previous sections, where the diagnostics of confined ions are described, this one is devoted to the measurements of the lost energetic ions. Several techniques to measure MHD induced fast-ion losses in magnetically confined fusion devices have been explored over the last decades with the most successful techniques based on charge particle collectors. Charge particle collectors (CPC) are located at the edge of the plasma and are therefore exposed to high heat load. Scintillators, Faraday cups and activation foils have been typically used to detect the escaping ions [186, 41, 179, 113, 75, 34, 78]. CPCs make used of the tokamak/stellarator magnetic field to disperse the escaping ions onto the detector active component with their strike point depending on the ion energy and pitch-angle having thus velocity-space resolution. The temporal, energy, and pitch-angle resolution depend ultimately on the detector active component and detailed design. Infra-red (IR) measurements are based on the heat load deposited by the escaping ions on the plasma facing components. The fast-ion IR measurement is complicated by the thermal heat load that is typically an order of magnitude higher. Dedicated experiments allow to decouple both thermal from supra-thermal heat loads. While local measurements such as CPCs normally have an excellent velocity-space coverage but with a spatial coverage limited to the detector position, IR measurements have an excellent spatial coverage without velocity-space resolution. The ideal fast-ion loss detector is composed by an array of CPCs spatially distributed over the entire first wall of the device and a set of wide angle IR cameras covering the entire first wall. In order to identify the MHD fluctuations responsible for the fast-ion losses, Alfvenic temporal resolution is required. In the following, the operational principle, standard resolution and capabilities and prospects towards future devices of a scintillator based FILD are presented.
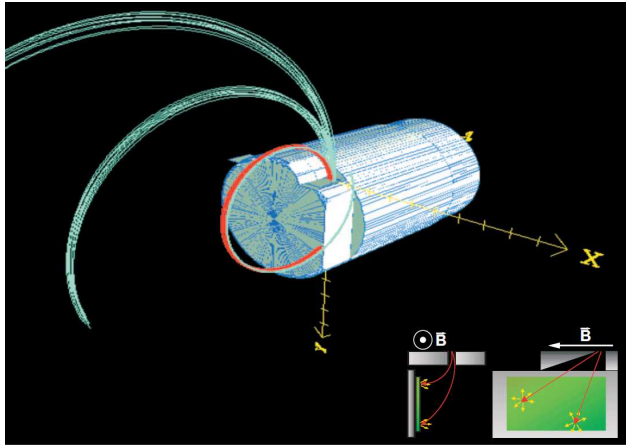
Fig. 25 FILD operational principle. CAD view of some escaping ion trajectories hitting the detector head. In blue particle trajectories which enter into the scintillator chamber and in red particle trajectories blocked by the graphite protection. The inset on the right-bottom part of the figure shows the collimating process. Figure taken from [41].

5.1 Operational principle

A scintillator based FILD [41] acts as a magnetic spectrometer, dispersing the measured escaping fast-ions onto the detector active component (scintillator and Faraday cup), with the strike points depending on their gyroradius (energy) and pitch-angle (angle between ion velocity and magnetic field line), thus, giving the full information of the velocity-space of the escaping ions at the detector position, see Fig. 25. A spatial array of detectors would then complete the phase-space information. The main constraints for fast-ion loss detection in fusion plasmas can be clustered into two groups: the geometrical constraints given by the shape of the first wall and the relative low particle radial drifts and the operation constraints imposed by the pulse length and harsh environments. While the passive components of the fast-ion loss detectors (electronic, lenses, light detection systems, etc.) are installed outside of the vacuum vessel and are thus common to other Fusion diagnostics, the active components of the detector (particle detection systems) operate close to the plasma edge and can be therefore strongly affected by the harsh environment. A throughout characterization of the response of the FILD active components to the impinging ions in a fusion relevant environment is therefore required to extract absolute fluxes of fast-ion losses from FILD systems. The complicated scintillator response to charge particles in a fusion relevant environment has prevented the community to provide absolute fluxes of measured fast-ion losses. Instead, Faraday cups embedded in FILD systems have been typically used to infer absolute fluxes from the measured fast-ion losses. Background currents induced by nuclear reactions in the Faraday cup system or electromagnetic pick-up signals complicate, however, this direct measurement at a fusion plasma. The absolute calibration of a FILD scintillator screen, have nevertheless, provide some of the most valuable absolute measurements of fast-ion losses in
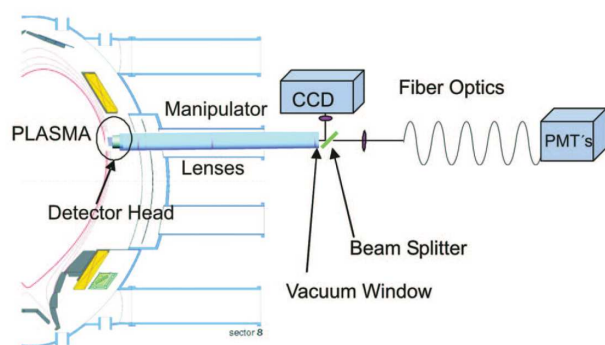
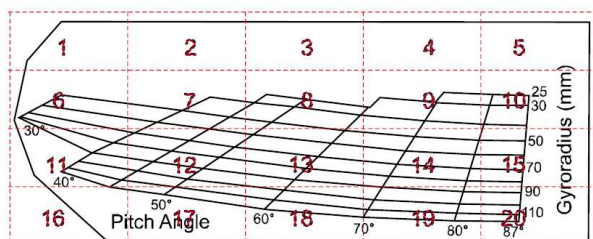**Fig. 26** ASDEX Upgrade FILD setup. Figure taken from [41].

Fig. 27 Strikemap of the ASDEX Upgrade FILD systems with PMT field of view overlayed. Figure taken from [41].

a tokamak. An instrument function that includes the scintillator efficiency, collimator geometry, optical transmission and camera efficiency has to be constructed for each setup.

5.2 FILD setup

As a CPC, FILD systems are composed of a charged particle detector, typically a scintillator, located close to the last closed flux surface. The light emitted by the scintillator is then transmitted through an optical system and imaged by a camera and an array of photomultipliers, see Fig. 26. The scintillator screen is protected against stray radiation and other ionizing particles by a graphite cup. The geometry of this graphite cup must be well designed in order to minimize secondary radiation without blocking the trajectories of the target particles. This design is typically done by means of Monte Carlo simulations that include the background magnetic field and 3D geometry of the detector head including collimator and scintillator. The simulated particle strike points on the scintillator for a given detector head geometry is then used to construct a strike map that helps identifying the energy and pitch-angle of the escaping ion, i.e. their orbit topology. The field of view of the FILD camera and PMT array are optimized to cover the entire strike map as Fig. 27 shows.
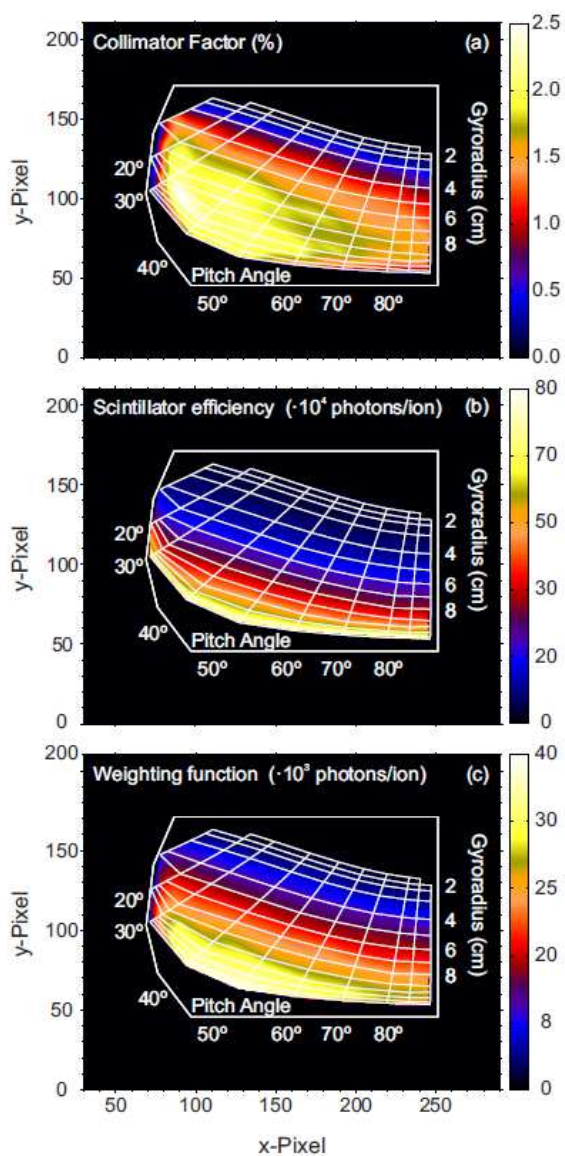
Fig. 28 (a) Collimator factor, (b) scintillator efficiency and (c) weighting function for the ASDEX Upgrade FILDs. Figure taken from [136].

5.3 The FILD instrument function

In order to obtain the distribution function of escaping ions hitting the aperture of the FILD head from the distribution on the scintillator, and thus the first wall, as well as the absolute flux of measured losses, an instrument function that includes the scin-
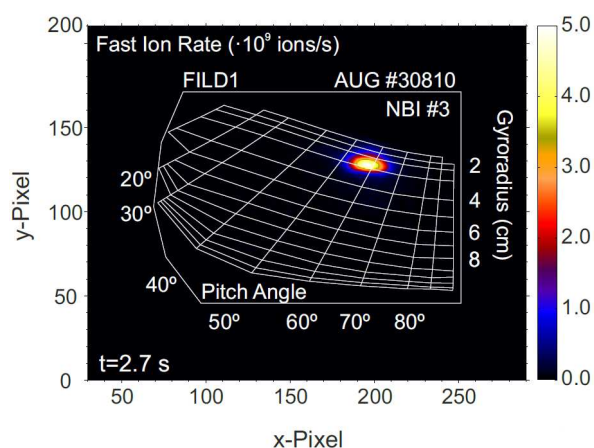
Fig. 29 Absolute fast-ion loss rate on the FILD scintillator screen. Figure taken from [136].

tillator efficiency, collimator geometry, optical transmission, and camera efficiency has to be constructed [136]. While the collimator factor only depends on the 3D geometry of the detector head, the scintillator efficiency depends on several parameters such as the particle species to be detected, the operation temperature and ion dose. Fig. 28 shows the typical collimator factor in an ASDEX Upgrade FILD system (a), the scintillator efficiency to deuterium ions (b) and convoluted weighting function (c). The weighting function is a convolution of the collimator factor and scintillator efficiency. The final instrument function is obtained from the actual measurement, the weighting function, optical transmission and efficiency of the light acquisition systems. Fig. 29 shows the absolute flux of measured fast-ion losses in velocity-space by a FILD system of the ASDEX Upgrade tokamak.

5.4 FILD measurement of MHD induced fast-ion losses

MHD induced fast-ion losses have been measured by FILD systems in virtually all major fusion devices. MHz sampling rates are used to identify the MHD fluctuations responsible for the observed fast-ion losses. While CCD cameras are used to obtain the velocity-space of the escaping ions with high resolution but moderate (ms) temporal resolution, the PMT array is used to identify the fluctuations responsible for the losses through Fast Fourier Transforms (FFT). Typical measurements of fast-ion losses induced by AEs in the ASDEX Upgrade tokamak are shown in Fig. 30 and Fig. 31. Fig. 30 shows the velocity-space of the measured AE induced fast-ion losses in an ICRF heated plasma at two different time points; in the presence of many AEs (a) and in the presence of a single AE (b). This information is used to calculate the orbit topology of the lost ion backwards in time in order to understand the wave-particle interaction that has caused this loss. This accurate velocity-space measurements are complemented with PMT based time-resolved measurements of the ion flux. These measurements not only allow the identification of the most deleteri-
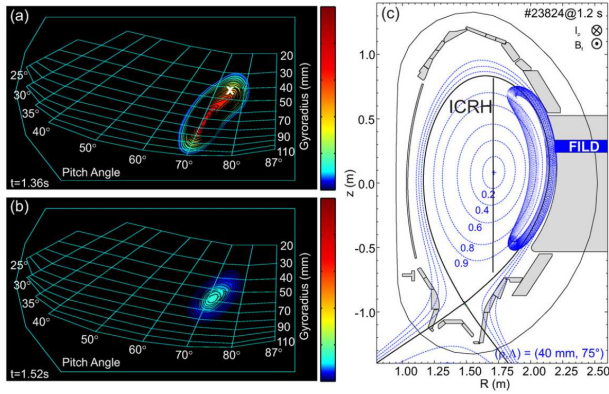
Fig. 30 (a) Velocity-space of escaping ions in the presence of (a) many AEs and (b) a single n = 5 AE. (c) Typical trajectory of a lost hydrogen ion with E = 200 keV calculated backward in time from detector collimator to the plasma. The vertical black line indicates the position of the ICRH resonance layer. Figure taken from [42].

ous MHD fluctuations for the fast-ion confinement but they also help to understand the wave-particle interactions underlying the observed fast-ion transport. Fig. 31 (a) shows a spectrogram of a FILD signal obtained in a plasma with AE induced fast-ion losses. Toroidally induced AEs (TAEs) and Reversed Shear AEs (RSAEs) are clearly visible in the FILD spectrogram. The raw data shown in Fig. 31 (b) shows, however, two different components in the FILD signals: a fluctuating signal, that produces the spectrogram of Fig. 31 (a) and a fairly constant signal. Extensive data analysis and theoretical efforts have been used to estimate the convective and diffusive character of MHD induced fast-ion losses based on such kind of FILD measurements.

5.5 Status of the ITER FILD

Although several diagnostics for confined fast-ions are being proposed for ITER, a lost alpha diagnostic has not been approved as of yet. The harsh environment in ITER – a nuclear machine – places a number of constraints on standard fast-ion loss detection techniques unprecedented on present tokamaks with easier access and more tolerable conditions. On the basis of the physics requirements and integration capabilities, the Port Plugs and Diagnostics Integration Division at ITER Organization has started to undertake a conceptual study of a reciprocating FILD system for ITER [47].

ASCOT simulations have been carried out to estimate the fast-ion flux on the ITER first wall. Externally applied 3D fields have been used to simulate the effect of MHD fluctuations on alpha particle transport and thus to estimate the detector signals in the presence of MHD fluctuations. The optimal detector position and measurement cycle are, in fact, given by the balance between the measured fast-ion signals and the heat load on the detector head. Based on these ASCOT simulations, a stroke of 20 cm is sufficient to keep the entire detector head behind the Diagnostic First Wall (DFW)
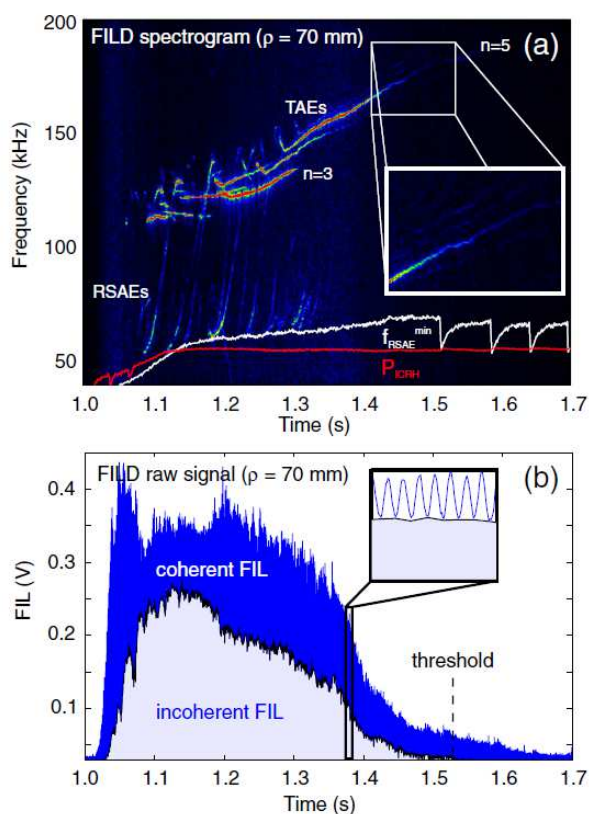
Fig. 31 (a) Power spectrogram of the fast-ion loss signal with gyroradius 70 mm. The inset shows the single TAE responsible for the onset of the incoherent losses. (b) Fast-ion loss signal. The coherent and incoherent components of the losses are highlighted. The vertical dashed line depicts the threshold for the incoherent losses. Figure taken from [43].

in a safe parking position as well as to deploy the detector aperture 11 cm outside of the DFW during measurements. In the present design, the scintillator plate is located approximately 2 cm behind the heat shield. Fig. 32 shows the expected alpha particle heat load on the ITER first wall. The total number of 10^6 test fusion born α-particles have been followed until they thermalize or hit the wall. The different wall structures of the low field side are clearly visible together with the n = 4 RMP structure. As expected, due to the ion grad-B drift, most losses appear at the divertor and mid-plane wall structures with a maximum heat load around $1\,MW/m^2$. The n = 4 RMP, caused by the ELM mitigation coils, has I_{coil} = 90 kA, has been used to simulate an extreme case with high but realistic alpha particle losses. Detailed heat load analysis including transient Edge Localized Modes (ELMs) losses and nuclear heating has shown that at the measurement position, the detector head will be exposed to heat loads similar to that in present large tokamaks. The nuclear heating suffered by the system during the entire discharge forces the design to include an active cooling system. The high neutron and gamma fluxes expected close to the ITER first wall lead also to back-
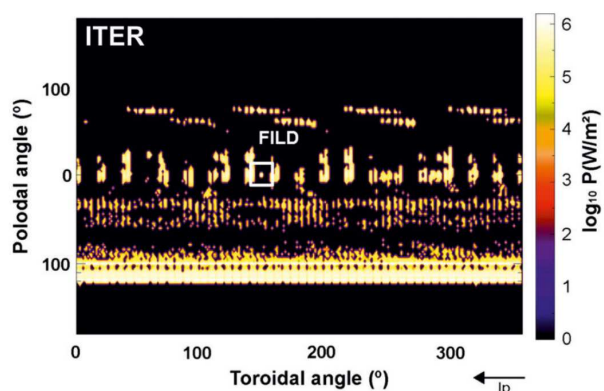
Fig. 32 ASCOT simulations of alpha particle heat load in ITER on a 3D first wall due to an externally applied n = 4 RMP. The location of the FILD head is indicated with a white box. Figure taken from [47].
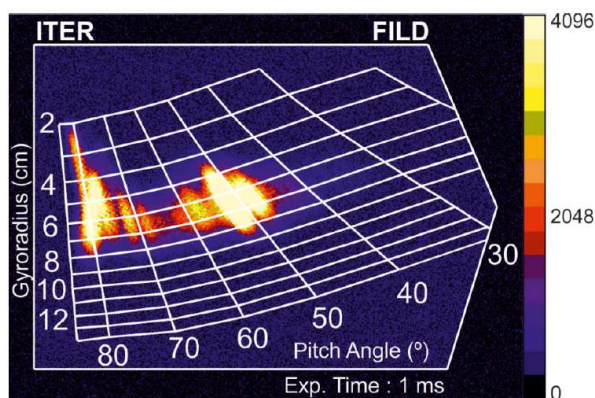

Fig. 33 Synthetic measurement of alpha particle losses induced by RMPs with the present design of the ITER FILD. Figure taken from [47].

ground scintillator emission that could, if not designed properly, hamper the FILD measurements at ITER.

Preliminary calculations show that the MHD induced alpha particle signals expected in ITER are well above the background signals produced by neutron and gamma fluxes. Fig. 33 shows a synthetic measurement of alpha particle losses induced by a n=4 externally applied RMP including background emission produced in the scintillator by charge particles born nuclear reactions.

6 Measurements of fast-ion velocity distribution functions: From velocity-space sensitivity to tomography

The traditional way to analyze fast-ion measurements is to compare the actual measurements with synthetic meaurements based on numeric simulations. Examples for this method abound in the literature for CTS [139, 106, 112, 132], fast-ion D_α spectroscopy (FIDA) [59, 60, 52], neutron emission spectrometry (NES) [62, 64, 28, 151] and γ-ray spectrometry (GRS) [84, 172, 120]. Agreement between synthetic measurements and actual measurements is taken as indication that the simulated fast-ion phase-space distribution function is a good model for the fast ion population in the plasma. However, often measurements and simulations disagree. In this case it is difficult to tell from the measurements what causes the discrepancies and what this actually means for the fast-ion phase-space distribution function. In this section we discuss methods to connect fast-ion measurements with the fast-ion velocity distribution function.

6.1 Velocity-space sensitivity of fast-ion diagnostics

The first step to learn about the velocity distribution function is to assess the velocity-space sensitivity of the various fast-ion diagnostics. This idea was developed as a qualitative analysis tool to understand a puzzling observation in an experiment at DIII-D [60]. The FIDA measurements and the neutron count measurements behaved in a very similar way whereas the NPA measurements behaved qualitatively differently. This was at the time surprising because the NPA and FIDA monitor neutrals generated in the same charge-exchange reaction. FIDA measures the D_α-light emitted by the neutrals, and NPA measures the neutrals that do not re-ionize on the path to the detector. Therefore the NPA signal was (mistakenly) expected to behave in a qualitatively similar way as the FIDA signal. However, the velocity space observation region of FIDA and the neutron count measurement are broad regions in velocity space, and they are fairly similar, whereas the NPA observes a tiny region in velocity space which was illustrated by so-called weight functions. This new understanding of the velocity-space observation regions then resolved this at the time puzzling observation. Since then weight functions have been developed for all major fast-ion diagnostics: FIDA [60, 143], neutral particle analyzers (NPA) [60], CTS [140], fast-ion loss detectors [129], NES [69, 72, 73] and GRS [145, 148].

In a general definition valid for any diagnostic, weight functions, w, relate measurements, s, to 2D fast-ion distribution functions, f, by the integral equation [60, 57, 140, 143, 69, 72, 73, 145, 148]

$$s(m_1, m_2, \phi) = \int_{vol} \int_0^\infty \int_{-\infty}^\infty w(m_1, m_2, \phi, v_\parallel, v_\perp, \mathbf{x}) f(v_\parallel, v_\perp, \mathbf{x}) dv_\parallel dv_\perp d\mathbf{x}. \tag{11}$$

$s(m_1, m_2, \phi)$ is the detected signal in the measurement range $m_1 < m < m_2$ with a viewing angle ϕ between the line-of-sight of the diagnostic and the magnetic field. $(v_\parallel, v_\perp)$ are the velocities parallel and perpendicular to the magnetic field, respectively, and $\mathbf{x}$ describes the spatial coordinates. The units of f in equation 11 are

[s^2/m^5]. The units of weight functions are thus [signal / fast ion] where the units of the signal are particular to each instrument.

Weight functions are routinely found numerically for any diagnostic using a forward model that predicts the measured signal for an arbitrary fast-ion distribution function. In this numerical approach, the signal s due to N_f fast ions is calculated for a grid of velocities $(v_\parallel, v_\perp)$ or (E, p) covering the target velocity space region. The velocity distribution function of the N_f fast ions at phase-space position $(\mathbf{x}_0, v_{\parallel 0}, v_{\perp 0})$ is

$$f(v_\parallel, v_\perp, \mathbf{x}) = N_f \delta(v_\parallel - v_{\parallel 0}) \delta(v_\perp - v_{\perp 0}) \delta(\mathbf{x} - \mathbf{x}_0). \qquad (12)$$

Substitution into equation 11 and integration shows that the amplitudes of weight functions at phase-space position $(\mathbf{x}_0, v_{\parallel 0}, v_{\perp 0})$ are readily computed from

$$w(m_1, m_2, \phi, v_{\parallel 0}, v_{\perp 0}, \mathbf{x}_0) = \frac{s(m_1, m_2, \phi)}{N_f}. \qquad (13)$$

Weight functions hence show the integrated signal between two spectral points per ion at phase-space position $(\mathbf{x}_0, v_{\parallel 0}, v_{\perp 0})$. The shapes of the weight functions of the various diagnostics has been understood by considering the underlying physical processes for[140, 143, 73, 145, 148]. In velocity space $(v_\parallel, v_\perp)$, FIDA and CTS observe triangular regions whereas NES and one-step reaction GRS observe regions bounded by circular arcs. Two-step reaction GRS observes fairly complicated regions whereas NPA observes tiny regions. Examples of weight functions for the major fast-ion diagnostics are illustrated in figures 34 to 39.
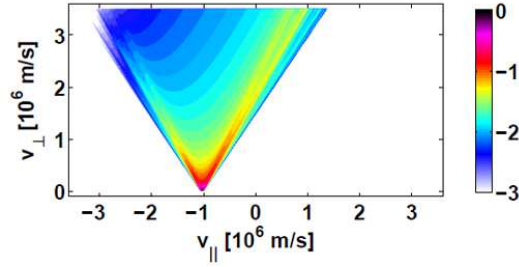

Fig. 34 Theoretical model of a FIDA weight function which looks similar to the CTS weight function from Fig. 35. The triangular shape comes from the Doppler shift. The bias towards the right comes from changing charge-exchange probabilities along the gyro-orbit. The fringing at the boundaries comes from Stark splitting. The figure is taken from [143].

This understanding of velocity-space sensitivities allows five types of data analysis. First, the observable and the unobservable velocity space can be told apart. Second, given a 2D fast-ion velocity distribution function, the velocity distribution of the ions generating a given measurement can be calculated. Third, given the absence of a measurement signal, the corresponding empty region of velocity space can be identified. Fourth, synthetic measurements can be calculated rapidly. Fifth, we can infer 2D fast-ion velocity distribution functions by velocity-space tomography which we will discuss in the next section.
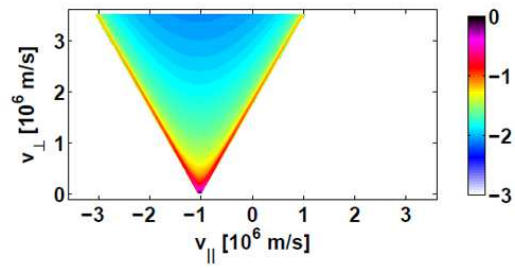
Fig. 35 CTS weight functions have a triangular shape due to the Doppler shift. The opening angle is $2\,\phi$, and the closest distance to the origin is the projected velocity u. The figure is taken from [143]
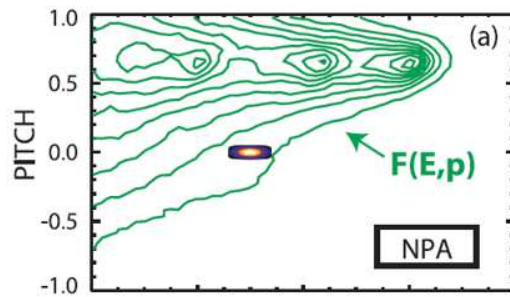

Fig. 36 The NPA weight function covers a small region in velocity space since the the the gyrophase is fixed to a small range by the geometry of the measurement. The figure is taken from [60].
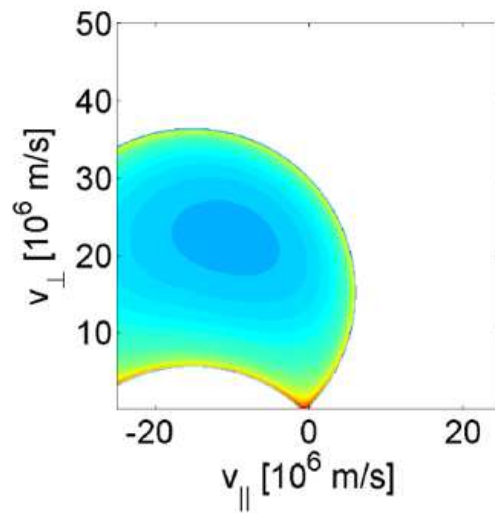

Fig. 37 NES weight functions are bounded by circular arcs. Their shape is determined by conservation of energy and momentum. The figure is taken from [73].
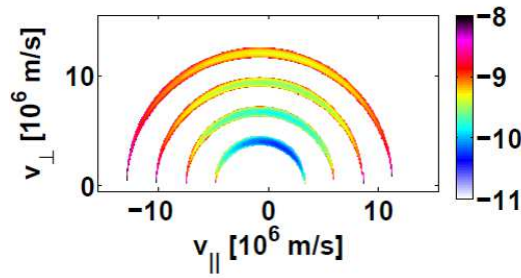
Fig. 38 GRS weight functions for four different Doppler shifts. This type of weight function has energy resolution as the form of the weight function is close to concentric circles. The figure is taken from [148]
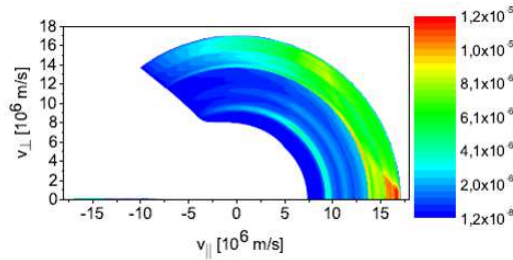

Fig. 39 GRS weight function for two-step reactions. The figure is taken from [145].

6.2 Velocity-space tomography and the combination of fast-ion diagnostics

Velocity-space tomography is a method to obtain a 2D image of the fast-ion velocity distribution function based on the available fast-ion measurements [26, 140–142, 144, 146, 51, 178, 70, 71, 74, 133]. This 2D image is the best useful fit to all available measurements from the available diagnostics. The spectra contain often hundreds of data points, and this large amount of data is difficult to exploit by traditional means, also considering that each data point observes a different region in velocity space. Furthermore, the data is usually presented in particular diagnostic units that are difficult to interpret for outsiders to the particular diagnostic, such as experts from other fast-ion diagnostics or the simulation community. The 2D image produced by velocity-space tomography, on the contrary, is straightforward to interpret and shows directly the fast-ion velocity distribution function which is the fundamental quantity of interest that is known to most workers. Another advantage of this inversion method is that nuisance parameters are accounted for whereas the diagnostic spectra also depend on nuisance parameters. For example, the amplitude of measured spectra during a sawtooth crash decreases if the ion density decreases. The method has become possible due to the weight function formalism discussed in the previous section. The tomographic inversion of the fast-ion measurements can be directly compared with numerical simulations and hence provides an alternative meeting ground between theory and observation.

Discretization of equation 11 allows us to reformulate the forward model of a given fast-ion diagnostic as the matrix equation

$$S = WF \qquad (14)$$

where F is the fast-ion velocity distribution function rearranged as column vector, S is a column vector holding the measurements, and W is a matrix holding the weight functions rearranged as lines [141]. To take the measurement uncertainty of the individual data points into account, both sides of each line of the equation system are divided by the uncertainty. This step also allows the combination of various diagnostics as it normalizes the S vector to become a signal-to-noise ratio vector where all entries have similar magnitudes which improves the conditioning of the problem [142]. The problem to determine F from S is now to find a useful inversion of W. Due to noise in the measurements, however, this problem has no solution, and instead one computes a least-squares fit. As the weight matrix W is ill-conditioned, noise in the measurements makes it necessary to add some form of regularization to the problem as is done in standard position-space tomography. To date velocity-space tomography has employed the standard inversion methods singular value decomposition (SVD), the maximum entropy method, and variants of the Tikhonov regularization [144,146, 178,70]. Compared with many other tomography applications, the amount of measurement data is small due to the limited optical access to the plasma and the often comparatively small signal-to-noise ratio. Inversions are for this reason often plagued by artifacts. Artifacts can be reduced by optimizing the discharges. For FIDA usually L-mode plasmas with low density and low heating power work well [144,51, 178,70]. The installation of additional fast-ion diagnostics is a very effective remedy against artifacts [141,178]. High-definition tomography techniques make use of additional prior information one might have which also decreases artifacts and improves the inversions [147]. Potent prior information are the measured absence of ions, the position of the injection sources in velocity space, the non-negativity constraint, the smoothness of the velocity distribution function, or, if available, a numeric simulation of the discharge [147]. These high-definition tomography techniques improved results for the five-view FIDA diagnostic at the tokamak ASDEX Upgrade and further allow the use of inversion techniques for more common FIDA systems with two or three views. The recent inversion of GRS and NES measurement data at JET also relied on these techniques [149]. As an example we show the formulation as a Tikhonov problem with non-negativity constraint:

$$F^* = \arg\min_F \left\| \begin{pmatrix} W \\ \lambda L \end{pmatrix} F - \begin{pmatrix} S \\ 0 \end{pmatrix} \right\|_2 \qquad \text{subject to} \quad F^* \geq 0 \qquad (15)$$

Here the upper row minimizes the residual of the original least square problem. The lower row penalizes the size of LF where L is the regularization matrix which is often chosen to effect a gradient in discrete form. In this case the lower row penalizes steep gradients and forces the solution to the problem to be smooth. The regularization parameter λ must be found as part of the solution and balances the requirement to fit the data and the smoothness requirement. The combination of fast-ion diagnostics has been demonstrated using FIDA and CTS [142,71,133] and GRS and NES based on time-of-flight detection, single-crystal diamonds and liquid organic scintilator [149]

6.3 Experimental results of velocity-space tomography

Velocity-space tomography has provided measurements of NBI- and ICRF fast-ion velocity distribution functions. Good agreement between the measured fast-ion velocity distribution functions and TRANSP simulations was found for an NBI heated plasma at ASDEX Upgrade in the absence of strong magnetohydrodynamic (MHD) activity [144,178]. Profiles of the fast-ion velocity distribution function from the plasma center towards the edge have been measured at ASDEX Upgrade [177]. The method has also recently revealed velocity-space redistribution patterns of fast ions due to sawtooth crashes at ASDEX Upgrade [51,178,70,71,147,74,133]. Measured velocity distribution functions in the plasma center at ASDEX Upgrade before and after a sawtooth crash are illustrated in figure 40.
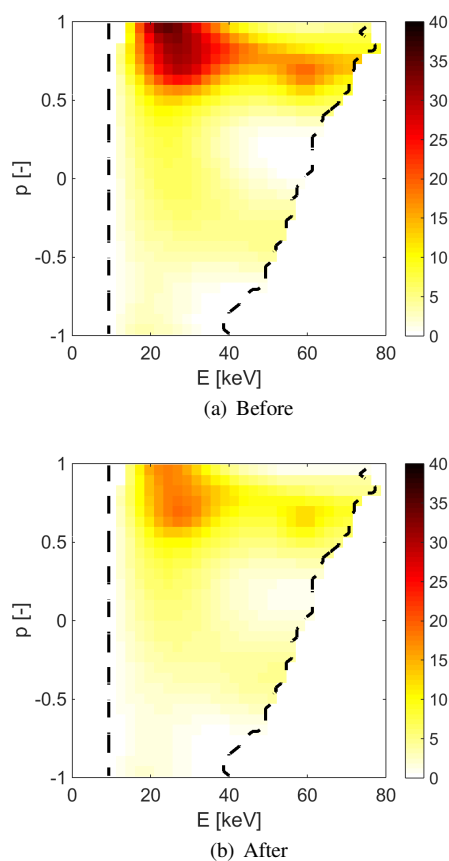

(a) Before

(b) After

Fig. 40 Measurements of the fast-ion velocity distribution function in the plasma center at ASDEX Upgrade discharge #32323 before and after a sawtooth crash [147].

The zeroth moment of the fast-ion velocity distribution function provides the fast-ion density which is thought to be an important parameter. The ITER measurement requirements for fast-ion diagnostics ask for measurements of the fast-ion or alpha densities and energy spectra. These important parameters can be measured by velocity-space tomography without assuming any model for the fast-ion velocity distribution function, such as a slowing-down distribution. Figure 41 compares measured time traces of the fast-ion density in a sawtoothing ASDEX Upgrade plasma with a corresponding TRANSP simulation. The TRANSP simulation predicts somewhat more violent sawtooth crashes than supported by the measurements. Velocity-space tomography further allows us to study phase-space densities such as the densities in different pitch ranges which is also illustrated in figure 41. A qualitative difference appears for pitches $p < 0.25$ where no evidence for sawteeth is found in the FIDA data. However, the TRANSP simulation does predict sawteeth in this pitch range as for the other pitches. The rich FIDA data in this discharge could be efficiently summarized in a movie of the velocity distribution function measured by velocity-space tomography which is available as supplementary material to reference [147]. The time resolution of the movie was 2 ms.
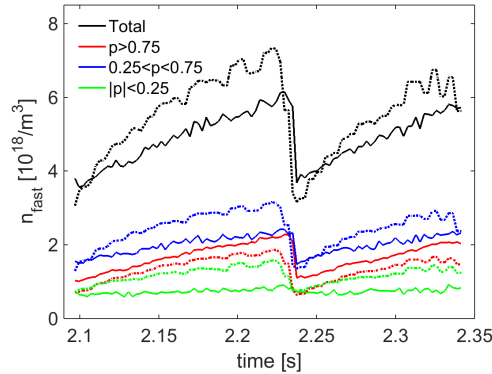

Fig. 41 Measured and simulated fast-ion densities in AUG #32323 [147]

Energetic ions in the MeV-range have been studied at JET by velocity-space tomography. The energetic ions were generated by 3 MW of ICRF at the third harmonic of deuterium and 4.5 MW of NBI. The ICRF accelerates the NBI ions from below 120 keV to 2 MeV. Measurements were done with a HpGe GRS detector providing spectral resolution of two gamma-ray peaks as well as three NES detectors: TOFOR, a single-crystal diamond detector, and a liquid scintilator detector. Figure 42 shows a comparison of the tomographic inversion of these measurements and a numerical simulation. The length and width of the fast-ion tail were found to be in excellent agreement including the presence of the barrier region that does not permit acceleration to energies larger than 2 MeV [151] and the thickening of the tail towards lower velocities due to collisions. ICRF acceleration of NBI ions above the injection energy was also recently demonstrated at ASDEX Upgrade [177].
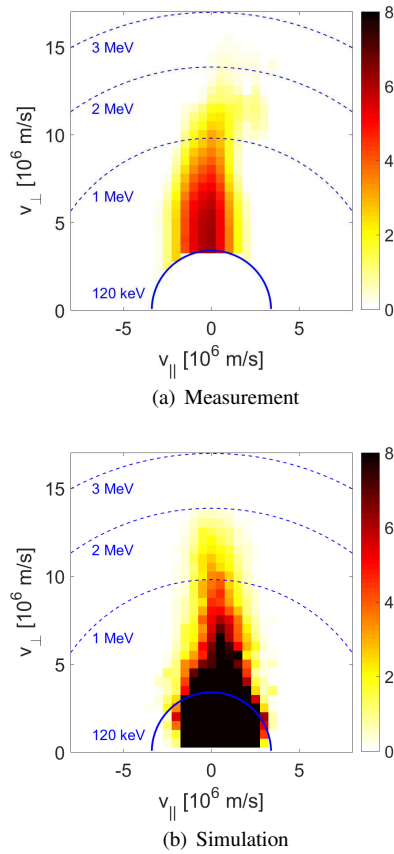
Fig. 42 Measurement and simulation of an MeV-range ion velocity distribution function at JET [149]

7 Conclusions

Fusion devices are equipped with a number of diagnostics probing various parts of the fast-ion phase-space distribution function. Key fast-ion diagnostics are NES, GRS, CTS, FIDA, NPA, and FILD. Confined fast ions are difficult to diagnose due to the limited access to the plasma and the usually low signal-to-noise ratio. Nevertheless, recent advances in the various diagnostic methods have allowed fast-ion measurements with unprecedented levels of detail, allowing us to validate and confront our understanding of fast-ion physics.

Both NES and GRS diagnostics measure the products of nuclear reactions which only occur if at least one of the reactants is energetic. Neutron diagnostics can be divided into the neutron counters and neutron spectrometers. Neutron counters are compact and can be installed at several locations which allows a generally accurate reconstruction of the emission profiles. Neutron spectrometers are bulky, but the size is essential to retrieve accurate information that is required to study the suprather-

mal populations of the fuel ions. The most successful instruments are based either on time-of-flight or magnetic proton recoil techniques. Recently developed diamond detectors allow compact neutron spectrometers in the future, but now the quality of the data from conventional neutron spectrometers is superior.

GRS is based on two different reactions: one- and two-step gamma reaction. The one-step gamma-reaction has a small cross-section and therefore a worse signal-to-noise ratio. The detection of the gamma radiation is done by using scintillator crystals, where high-energy photons induce luminescence in the visible spectrum. Recent advances in the development of fast, high resolution scintillators make the detectors suitable for applications in environments with large neutron fluxes, such as DT fusion experiments.

Both NES and GRS will be installed on ITER, where they benefit from increased neutron and gamma-ray fluxes, thanks to the larger size and higher fusion performance of this machine. The design of the set-up is similar to the one used at JET now.

Active NPA and FIDA are based on the charge-exchange. Both diagnostics rely on substantial densities of neutral atoms in the plasma core. In modern fusion experiments the neutrals are supplied by NBI. NPA measures escaped neutrals from the plasma that are born in the charge-exchange process between fast ions and injected neutral atoms. The diagnostic has a very good signal-to-noise ratio and extremely high dynamic range, over six orders of magnitude in some devices. The spatial resolution and in particular the velocity-space resolution of active NPAs is very good. FIDA is based on a spectroscopy of the broadened Balmer-alpha line in the same charge-exchange reaction. The diagnostic allows localized measurements from different lines-of-sight which allows the reconstruction of 2D velocity distribution functions. Additionally, profile measurements are possible by an array of lines-of-sight. While the diagnostic works very well in low-density plasmas with ion energies below 200 keV, the diagnostic of MeV range ions is hampered by the very low charge-exchange cross-sections at high energies. High-density plasma further leads to a poor beam penetration and high levels of bremsstrahlung which makes an implementation at ITER challenging.

Information on the projection of the fast ion velocity distribution function is encoded in the scattering spectrum of the CTS diagnostic. The diagnostic in modern machines is flexible and allows spatially resolved measurements with the different resolved angles. Besides the information on fast ions, the scattering signal contains signatures of the MHD activity and various waves in the plasma, etc. This makes the inference of the fast ion velocity distribution function challenging. Often long integration times are needed in order to receive a spectrum with good signal-to-noise ratio. The diagnostic is planned for ITER, where it will probe fusion-born and NBI-originated fast ions at seven spatial locations.

The fast ion loss detectors are used for the measurements of lost energetic ions. They are capable of resolving the loss in the phase space, they have high dynamic range and sensitivity, thus allowing measurements with high temporal resolution. The information provided by FILD systems has been key to understand the wave-particle interactions responsible for the observed MHD induced fast-ion losses in present devices. Preliminary studies for the integration of a FILD system in ITER are quite encouraging though further work is still necessary.

Currently there is no diagnostic alone which is capable of resolving the entire confined fast-ion phase-space distribution function. However, the measurement signals of the various diagnostics can be related to the phase-space distribution function by so-called weight functions. This allows an integrated data analysis of the available fast-ion diagnostics by formulating an inversion problem that can be solved by standard methods of usual position-space tomography. Using prior information the velocity distribution function can now be reconstructed by velocity-space tomography. A combination of confined fast ions diagnostics is used for the reconstruction of the velocity distribution function on ASDEX Upgrade and most recently on JET. Efforts to implement similar approaches on other machines are on the way. Joint experiments within the International Tokamak Physics Activity (ITPA) framework will test the approach on other machines with the goal to eventually combine fast-ion measurements on ITER.

Acknowledgments

References

1. Afrosimov, V.: Soviet physics. Technical physics **5**, 1378 (1961)
2. Allison, S.: Rev. Mod. Phys. **30**, 1137–1168 (1958). DOI 10.1103/RevModPhys.30.1137
3. Arvis O.: Plasma Phys. Control. Fusion **36**, 209 (1994). DOI 10.1088/0741-3335/36/2/002
4. Behn, R. *et al.*: Physical Review Letters **62**(24), 2833–2836 (1989). DOI 10.1103/PhysRevLett.62.2833
5. Berk, H.L. *et al.*: Phys. Rev. Lett. **87**, 185,002 (2001). DOI 10.1103/PhysRevLett.87.185002
6. Bindslev, H.: Ph.D. thesis, Risø National Laboratory (1992)
7. Bindslev, H.: Journal of Atmospheric and Terrestrial Physics **58**(8), 983–989 (1996). DOI 10.1016/0021-9169(95)00129-8
8. Bindslev, H.: Review of Scientific Instruments **70**(1), 1093 (1999). DOI 10.1063/1.1149521
9. Bindslev, H. *et al.*: Physical Review Letters **83**(16), 3206–3209 (1999). DOI 10.1103/PhysRevLett.83.3206
10. Bindslev, H. *et al.*: Review of Scientific Instruments **75**(10), 3598 (2004). DOI 10.1063/1.1779620
11. Bindslev, H. *et al.*: Physical Review Letters **97**(20), 205,005 (2006). DOI 10.1103/PhysRevLett.97.205005
12. Bindslev, H. *et al.*: Plasma Physics and Controlled Fusion **49**(12B), B551–B562 (2007). DOI 10.1088/0741-3335/49/12B/S52
13. Bortolon, A. *et al.*: The Review of scientific instruments **81**(10), 10D728 (2010). DOI 10.1063/1.3495768
14. Brysk, H.: Plasma Physics **15**(7), 611 (1973). DOI 10.1088/0032-1028/15/7/001

15. Carolipio, E.M. *et al.*: Nuclear Fusion **42**(7), 853 (2002). DOI 10.1088/0029-5515/42/7/308
16. Cazzaniga C. *et al.*: Rev. Sci. Instrum. **84**, 123,505 (2013). DOI 10.1063/1.4847056
17. Cazzaniga C. *et al.*: Review of Scientific Instruments **85**(4), 043,506 (2014). DOI 10.1063/1.4870584
18. Cazzaniga C. *et al.*: Reveiw of Scientific Instruments **85**, 11E101 (2014). DOI 10.1063/1.4885356
19. Cazzaniga C. *et al.*: Nucl. Instrum. Meth. A **778**, 20 (2015). DOI 10.1016/j.nima.2015.01.002
20. Cecconello M. *et al.*: Rev. Sci. Instrum. **81**, 10D315 (2010). DOI 10.1063/1.3479038
21. Cecil F.E. and Newman D.E.: Nuclear Instruments and Methods in Physics Research **221**, 449 (1984). DOI 0.1016/0167-5087(84)90018-8
22. Chugunov I. *et al.*: Instruments and Experimental Techniques **51**, 166 (2008). DOI 10.1134/S0020441208020024
23. Chugunov, I.N. *et al.*: Nuclear Fusion **51**(8), 083,010 (2011). DOI 10.1088/0029-5515/51/8/083010
24. Craciunescu T. *et al.*: Nucl. Instrum. Meth. A **605**, 374 (2009). DOI 10.1016/j.nima.2009.03.224
25. Duong, H.H. *et al.*: Nuclear Fusion **33**(5), 749 (1993). DOI 10.1088/0029-5515/33/5/I06
26. Egedal, J., Bindslev, H.: Physics of Plasmas **11**(5), 2191 (2004). DOI 10.1063/1.1697400
27. Erckmann, V. *et al.*: Fusion Science and Technology **52**(2), 291–312 (2007). DOI 10.13182/FST07-A1508
28. Eriksson, J. *et al.*: Nuclear Fusion **55**(12), 123,026 (2015). DOI 10.1088/0029-5515/55/12/123026
29. Eriksson J. *et al.*: Computer Physics Communications **199**, 40 (2016). DOI 10.1016/j.cpc.2015.10.010
30. Fasoli, A. *et al.*: Nuclear Fusion **47**(6), S264 (2007). DOI 10.1088/0029-5515/47/6/S05
31. Faust W.R., Harris E.G.: Nuclear Fusion **1**, 62–63 (1960). DOI 10.1088/0029-5515/1/1/006
32. Fehrenbacher G. *et al.*: Nucl. Instrum. Meth. A **372**, 239 (1996). DOI 10.1016/0168-9002(95)01289-3
33. Fernandes A. *et al.*: Fus. Eng. Des. **89**, 259 (2014). DOI 10.1016/j.fusengdes.2013.08.002
34. Fisher, R.K. *et al.*: Review of Scientific Instruments **81**(10), 10D307 (2010). DOI 10.1063/1.3490020
35. Fonck, R.: Review of Scientific Instruments **56**(5), 885–890 (1985). DOI 10.1063/1.1138033
36. Furtula, V. *et al.*: The Review of scientific instruments **81**(10), 10D913 (2010). DOI 10.1063/1.3478881
37. Furtula, V. *et al.*: The Review of scientific instruments **83**(1), 013,507 (2012). DOI 10.1063/1.3675886
38. G. Legge G. and Van der Merwe P.: Nuclear Instruments and Methods **63**, 157 (1968). DOI 10.1016/0029-554X(68)90321-2
39. García-Muñoz, M. *et al.*: Nuclear Fusion **47**(7), L10–L15 (2007). DOI 10.1088/0029-5515/47/7/L03
40. García-Muñoz, M. *et al.*: Nuclear Fusion **49**(8), 085,014 (2009)
41. García-Muñoz, M. *et al.*: Review of Scientific Instruments **80**(5), 053,503 (2009). DOI 10.1063/1.3121543
42. García-Muñoz, M. *et al.*: Nuclear Fusion **50**, 084,004 (2010). DOI 10.1088/0029-5515/50/8/084004
43. García-Muñoz, M. *et al.*: Physical Review Letters **104**, 185,002 (2010). DOI 10.1103/PhysRevLett.104.185002
44. García-Muñoz, M. *et al.*: Nuclear Fusion **51**(10), 103,013 (2011)
45. García-Muñoz, M. *et al.*: Nuclear Fusion **53**(12), 123,008 (2013). DOI 10.1088/0029-5515/53/12/123008
46. García-Muñoz, M. *et al.*: Plasma Physics and Controlled Fusion **55**(12), 124,014 (2013). DOI 10.1088/0741-3335/55/12/124014
47. García-Muñoz, M. *et al.*: Review of Scientific Instruments **87**, 11D829 (2016). DOI 10.1063/1.4961295
48. Gassner T. *et al.*: Physics of Plasmas **19**, 032,115 (2012). DOI 10.1063/1.3696858
49. Gatu Johnson, M. *et al.*: Nuclear Instruments and Methods in Physics Research Section A: Accelerators, Spectrometers, Detectors and Associated Equipment **591**(2), 417 – 430 (2008). DOI 10.1016/j.nima.2008.03.010
50. Geiger, B. *et al.*: The Review of scientific instruments **84**(11), 113,502 (2013). DOI 10.1063/1.4829481
51. Geiger, B. *et al.*: Nucl. Fusion **55**, 083,001 (2015). DOI 10.1088/0029-5515/55/8/083001
52. Geiger, B. *et al.*: Plasma Physics and Controlled Fusion **57**(1), 014,018 (2015). DOI 10.1088/0741-3335/57/1/014018

53. Geiger B., *et al.*: submitted to Plasma physics and controlled fusion (2017)
54. Glenzer, S.H.   *et al.*: Physical Review Letters **79**(7), 1277–1280 (1997).   DOI 10.1103/PhysRevLett.79.1277
55. Gorelenkov, N.N.   *et al.*: Nuclear Fusion **54**(12), 125,001 (2014).   DOI 10.1088/0029-5515/54/12/125001
56. Heidbrink, W., Sadler, G.: Nuclear Fusion **34**(4), 535–615 (1994). DOI 10.1088/0029-5515/34/4/I07
57. Heidbrink, W.W.: The Review of scientific instruments **81**(10), 10D727 (2010).   DOI 10.1063/1.3478739
58. Heidbrink, W.W. *et al.*: Nuclear Fusion **31**(9), 1635 (1991). DOI 10.1088/0029-5515/31/9/002
59. Heidbrink, W.W. *et al.*: Plasma Physics and Controlled Fusion **46**, 1855–1875 (2004).   DOI 10.1088/0741-3335/46/12/005
60. Heidbrink, W.W. *et al.*: Plasma Physics and Controlled Fusion **49**, 1457–1475 (2007).   DOI 10.1088/0741-3335/49/9/008
61. Heidbrink, W.W. *et al.*: COMMUNICATIONS IN COMPUTATIONAL PHYSICS **10**(3), 716–741 (2011). DOI 10.4208/cicp.190810.080211a
62. Hellesen, C. *et al.*: Plasma Physics and Controlled Fusion **52**(8), 085,013 (2010).   DOI 10.1088/0741-3335/52/8/085013
63. Hellesen, C. *et al.*: Nuclear Fusion **50**(8), 084,006 (2010). DOI 10.1088/0029-5515/50/8/084006
64. Hellesen, C. *et al.*: Nuclear Fusion **53**(11), 113,009 (2013). DOI 10.1088/0029-5515/53/11/113009
65. Hou, Y.M. *et al.*: Review of Scientific Instruments **87**(11), 11E552 (2016). DOI 10.1063/1.4960598
66. Hughes, T.P.   *et al.*: Journal of Plasma Physics **42**(2), 215–240 (1989).   DOI 10.1017/S0022377800014318
67. Isler, R.: Phys. Rev. Lett. **38**, 1359–1362 (1977). DOI 10.1103/PhysRevLett.38.1359
68. ITER Physics Expert Group: Nuclear Fusion **39**(12), 2471–2495 (1999).   DOI 10.1088/0029-5515/39/12/305
69. Jacobsen, A. S.   *et al.*: Review of Scientific Instruments **85**(11), 11E103 (2014).   DOI 10.1063/1.4885477
70. Jacobsen, A. S. *et al.*: Plasma Physics and Controlled Fusion **58**(4), 045,016 (2016).   DOI 10.1088/0741-3335/58/4/045016
71. Jacobsen, A. S. *et al.*: Plasma Physics and Controlled Fusion **58**(4), 042,002 (2016).   DOI 10.1088/0741-3335/58/4/042002
72. Jacobsen, A. S.   *et al.*: Review of Scientific Instruments **88**(7), 073,506 (2017).   DOI 10.1063/1.4991651
73. Jacobsen, A.S. *et al.*: Nuclear Fusion **55**(5), 053,013 (2015). DOI 10.1088/0029-5515/55/5/053013
74. Jaulmes, F *et al.*: Nucl. Fusion **56**, 112,012 (2016). DOI 10.1088/0029-5515/56/11/112012
75. Jimenez-Rey, D. *et al.*: Journal of Applied Physics **104**(6), 064,911 (2008). DOI 10.1063/1.2979327
76. Kaellne J. *et al.*: Phys. Rev. Letters **85**, 1246 (2000). DOI 10.1103/PhysRevLett.85.1246
77. Karpushov, A.N.   *et al.*: Review of Scientific Instruments **77**(3), 033,504 (2006).   DOI 10.1063/1.2185151
78. Kim, J. *et al.*: Review of Scientific Instruments **83**(10), 10D305 (2012). DOI 10.1063/1.4733550
79. Kimura, H. *et al.*: Nuclear Fusion **38**(9), 1303 (1998). DOI 10.1088/0029-5515/38/9/304
80. Kiptily V.: Nucl. Fusion **55**, 023,008 (2015). DOI 10.1088/0029-5515/55/2/023008
81. Kiptily, V.G. *et al.*: Nuclear Fusion **42**, 999–1007 (2002). DOI 10.1088/0029-5515/42/8/308
82. Kiptily, V.G. *et al.*: Nuclear Fusion **45**(5), L21–L25 (2005). DOI 10.1088/0029-5515/45/5/L01
83. Kiptily V.G. *et al.*: Plasma Phys. Control. Fusion **48**, R59 (2006). DOI 10.1088/0741-3335/48/8/R01
84. Kiptily, V.G. *et al.*: Nuclear Fusion **50**(8), 084,001 (2010). DOI 10.1088/0029-5515/50/8/084001
85. Kislyakov, A.I.   *et al.*: Plasma Physics and Controlled Fusion **43**(12), 1775 (2001).   DOI 10.1088/0741-3335/43/12/311
86. Knoll G.F.: Radiation Detection and Measurement. John Wiley and Sons, Inc. (2010)
87. Kolesnichenko, Y., Yakovenko, Y.: Nuclear Fusion **36**(2), 159 (1996).   DOI 10.1088/0029-5515/36/2/I04
88. Kondoh, T.   *et al.*: Review of Scientific Instruments **74**(3), 1642–1645 (2003).   DOI 10.1063/1.1532760
89. Kondoh, T. *et al.*: Plasma and Fusion Research **2**, S1111–S1111 (2007). DOI 10.1585/pfr.2.S1111
90. Korsholm, S B. *et al.*: In: 2016 41st International Conference on Infrared, Millimeter, and Terahertz waves (IRMMW-THz), pp. 1–2. IEEE (2016). DOI 10.1109/IRMMW-THz.2016.7758537
91. Korsholm, S.B. *et al.*: Nuclear Instruments and Methods in Physics Research Section A: Accelerators, Spectrometers, Detectors and Associated Equipment **623**(2), 677–680 (2010). DOI 10.1016/j.nima.2010.05.003

92. Korsholm, S.B. *et al.*: Phys. Rev. Lett. **106**(16), 165,004 (2011).   DOI 10.1103/PhysRevLett.106.165004
93. Kubo, S. *et al.*: The Review of scientific instruments **81**(10), 10D535 (2010).   DOI 10.1063/1.3481165
94. Lee, S., Kondoh, T.: In: 6th IAEA Technical Committee meeting on energetic particles in magnetic confinement systems, pp. 134–137. Naka, Japan (2000)
95. Leipold, F. *et al.*: The Review of scientific instruments **80**(9), 093,501 (2009).   DOI 10.1063/1.3212567
96. Leipold, F. *et al.*: In: 2016 41st International Conference on Infrared, Millimeter, and Terahertz waves (IRMMW-THz) (2016). DOI 10.1109/IRMMW-THz.2016.7758533
97. Machuzak, J.S. *et al.*: Review of Scientific Instruments **66**(1), 484 (1995). DOI 10.1063/1.1146323
98. Marushchenko, N.B. *et al.*: Computer Physics Communications **185**(1), 165–176 (2014). DOI 10.1016/j.cpc.2013.09.002
99. Medley, S.S. *et al.*: Review of Scientific Instruments **79**(1), 011,101 (2008). DOI 10.1063/1.2823259
100. Meo, F. *et al.*: The Review of scientific instruments **79**(10), 10E501 (2008). DOI 10.1063/1.2989140
101. Meo, F. *et al.*: Journal of Physics: Conference Series **227**, 012,010 (2010). DOI 10.1088/1742-6596/227/1/012010
102. Michael, C.A. *et al.*: Plasma Physics and Controlled Fusion **55**(9), 095,007 (2013).   DOI 10.1088/0741-3335/55/9/095007
103. Michelsen, S. *et al.*: Review of Scientific Instruments **75**(10), 3634 (2004). DOI 10.1063/1.1779611
104. Monte Carlo Code Group: Monte carlo n-particle code. URL https://mcnp.lanl.gov/
105. Moseev, D.: Phd thesis, Technical University of Denmark (2011)
106. Moseev, D. *et al.*: Plasma Physics and Controlled Fusion **53**(10), 105,004 (2011).   DOI 10.1088/0741-3335/53/10/105004
107. Moseev, D. *et al.*: In: 38th EPS Conference on Plasma Physics, p. P4.079 (2011)
108. Muscatello, C.M. *et al.*: The Review of scientific instruments **81**(10), 10D316 (2010). DOI 10.1063/1.3475367
109. Nielsen, S.K. *et al.*: Physical Review E **77**(1), 016,407 (2008). DOI 10.1103/PhysRevE.77.016407
110. Nielsen, S.K. *et al.*: Plasma Physics and Controlled Fusion **52**(9), 092,001 (2010).   DOI 10.1088/0741-3335/52/9/092001
111. Nielsen, S.K. *et al.*: Nuclear Fusion **51**(6), 063,014 (2011). DOI 10.1088/0029-5515/51/6/063014
112. Nielsen, S.K. *et al.*: Plasma Physics and Controlled Fusion **57**(3), 035,009 (2015).   DOI 10.1088/0741-3335/57/3/035009
113. Nishiura, M. *et al.*: Review of Scientific Instruments **75**(10), 3646–3648 (2004).   DOI 10.1063/1.1779606
114. Nishiura, M. *et al.*: Journal of Physics: Conference Series **227**, 012,014 (2010). DOI 10.1088/1742-6596/227/1/012014
115. Nishiura, M. *et al.*: Nuclear Fusion **54**(2), 023,006 (2014). DOI 10.1088/0029-5515/54/2/023006
116. Nocente, M.: Neutron and gamma ray emission spectroscopy as fast ion diagnostics in fusion plasmas. Ph.D. thesis, Universiti di Milano-Bicocca (2012)
117. Nocente M. *et al.*: Nucl. Fusion **50**, 055,001 (2010). DOI 10.1088/0029-5515/50/5/055001
118. Nocente, M. *et al.*: Review of Scientific Instruments **81**(10), 10D321 (2010).   DOI 10.1063/1.3501386
119. Nocente, M. *et al.*: Nuclear Fusion **52**(9), 094,021 (2012). DOI 10.1088/0029-5515/52/9/094021
120. Nocente, M. *et al.*: Nuclear Fusion **52**(6), 063,009 (2012). DOI 10.1088/0029-5515/52/6/063009
121. Nocente M. *et al.*: Nuclear Fusion **53**, 053,010 (2013). DOI 10.1088/0029-5515/53/5/053010
122. Nocente, M. *et al.*: IEEE Transactions on Nuclear Science **60**(2), 1408–1415 (2013). DOI 10.1109/TNS.2013.2252189
123. Nocente M. *et al.*: Nuclear Fusion **54**, 104,010 (2014). DOI 10.1088/0029-5515/54/10/104010
124. Nocente, M. *et al.*: Review of Scientific Instruments **86**(10), 103,501 (2015).   DOI 10.1063/1.4931755
125. Nocente M. *et al.*: Rev. Sci. Instrum. **87**, 11E714 (2016). DOI 10.1063/1.4961073
126. Nocente M. *et al.*: Nucl. Fusion **57**, 076,016 (2017). DOI 10.1088/1741-4326/aa6f7d
127. Orsitto, F. *et al.*: Review of Scientific Instruments **70**(1), 1158 (1999). DOI 10.1063/1.1149428
128. Osakabe, M. *et al.*: The Review of scientific instruments **79**(10), 10E519 (2008). DOI 10.1063/1.2968695
129. Pace, D C *et al.*: Rev. Sci. Instrum. **83**(7), 073,501 (2012). DOI 10.1063/1.4731655
130. Pinches, S.D. *et al.*: Physics of Plasmas **22**(2), 021,807 (2015). DOI 10.1063/1.4908551

131. Proverbio I. *et al.*: Rev. Sci. Instrum. **81**, 10D320 (2010). DOI 10.1063/1.3502037
132. Rasmussen, J. *et al.*: Plasma Physics and Controlled Fusion **57**(7), 075,014 (2015). DOI 10.1088/0741-3335/57/7/075014
133. Rasmussen, J. *et al.*: Nucl. Fusion **56**, 112,014 (2016). DOI 10.1088/0029-5515/56/11/112014
134. Richards, R. K. *et al.*: Applied Physics Letters **62**(1), 28–30 (1993). DOI 10.1063/1.108808
135. Rigamonti D. *et al.*: Rev. Sci. Instrum. **87**, 11E717 (2016). DOI 10.1063/1.4961060
136. Rodriguez-Ramos, M.: Plasma Phys. Control. Fusion **XX**, XXX (2017)
137. Ross, J.S. *et al.*: Physical Review Letters **104**(10), 105,001 (2010). DOI 10.1103/PhysRevLett.104.105001
138. Salewski, M. *et al.*: Nuclear Fusion **49**(2), 025,006 (2009). DOI 10.1088/0029-5515/49/2/025006
139. Salewski, M. *et al.*: Nuclear Fusion **50**(3), 035,012 (2010). DOI 10.1088/0029-5515/50/3/035012
140. Salewski, M. *et al.*: Nuclear Fusion **51**(8), 083,014 (2011). DOI 10.1088/0029-5515/51/8/083014
141. Salewski, M. *et al.*: Nuclear Fusion **52**(10), 103,008 (2012). DOI 10.1088/0029-5515/52/10/103008
142. Salewski, M. *et al.*: Nuclear Fusion **53**(6), 063,019 (2013). DOI 10.1088/0029-5515/53/6/063019
143. Salewski, M. *et al.*: Plasma Physics and Controlled Fusion **56**(10), 105,005 (2014). DOI 10.1088/0741-3335/56/10/105005
144. Salewski, M. *et al.*: Nuclear Fusion **54**(2), 023,005 (2014). DOI 10.1088/0029-5515/54/2/023005
145. Salewski, M. *et al.*: Nuclear Fusion **55**(9), 093,029 (2015). DOI 10.1088/0029-5515/55/9/093029
146. Salewski, M. *et al.*: Plasma Physics and Controlled Fusion **57**(1), 014,021 (2015). DOI 10.1088/0741-3335/57/1/014021
147. Salewski, M. *et al.*: Nucl. Fusion **56**, 106,024 (2016). DOI 10.1088/0029-5515/56/10/106024
148. Salewski, M. *et al.*: Nuclear Fusion **56**(4), 046,009 (2016). DOI 10.1088/0029-5515/56/4/046009
149. Salewski, M. *et al.*: Nuclear Fusion **57**, 056,001 (2017). DOI 10.1088/1741-4326/aa60e9
150. Salpeter, E.E.: Electron Density Fluctuations in a Plasma. Physical Review **120**(3), 1528 (1960). DOI 10.1103/PhysRev.120.1528
151. Schneider, M *et al.*: Nucl. Fusion **56**, 112,022 (2016). DOI 10.1088/0029-5515/56/11/112022
152. Schneider, P.A. *et al.*: The Review of scientific instruments **86**(7), 073,508 (2015). DOI 10.1063/1.4926886
153. Shalashov A.G. *et al.*: Plasma Physics and Controlled Fusion **45**(4), 395–412 (2003). DOI 10.1088/0741-3335/45/4/306
154. Sharapov, S.E. *et al.*: Physics Letters A **289**, 127 (2001). DOI 10.1016/S0375-9601(01)00588-6
155. Sharapov, S.E. *et al.*: Nuclear Fusion **53**(10), 104,022 (2013). DOI 10.1088/0029-5515/53/10/104022
156. Shimozuma, T.: Fusion Science and Technology **58**(1), 530–538 (2010). DOI 10.13182/FST58-530
157. Shinohara, K. *et al.*: Plasma Physics and Controlled Fusion **46**(7), S31 (2004). DOI 10.1088/0741-3335/46/7/S03
158. Sjostrand H. *et al.*: Rev. Sci. Instrum. **77**, 10E717 (2006). DOI 10.1063/1.2336459
159. Snipes, J.A. *et al.*: Physics of Plasmas **12**(5), 056,102 (2005). DOI 10.1063/1.1865012
160. Speth, E.: Reports on Progress in Physics **52**(1), 57 (1989)
161. Stejner, M. *et al.*: Review of Scientific Instruments **81**(10), 10D515 (2010). DOI 10.1063/1.3475540
162. Stejner, M. *et al.*: Plasma Physics and Controlled Fusion **53**(6), 065,020 (2011). DOI 10.1088/0741-3335/53/6/065020
163. Stejner, M. *et al.*: Plasma Physics and Controlled Fusion **54**(1), 015,008 (2012). DOI 10.1088/0741-3335/54/1/015008
164. Stejner, M. *et al.*: The Review of scientific instruments **83**(10), 10E307 (2012). DOI 10.1063/1.4729503
165. Stejner, M. *et al.*: Nuclear Fusion **52**(2), 023,011 (2012). DOI 10.1088/0029-5515/52/2/023011
166. Stejner, M. *et al.*: Plasma Physics and Controlled Fusion **55**(8), 085,002 (2013). DOI 10.1088/0741-3335/55/8/085002
167. Stejner, M. *et al.*: The Review of scientific instruments **85**(9), 093,504 (2014). DOI 10.1063/1.4894199
168. Stejner, M. *et al.*: Plasma Physics and Controlled Fusion **57**(6), 062,001 (2015). DOI 10.1088/0741-3335/57/6/062001
169. Stejner, M. *et al.*: In: 2016 41st International Conference on Infrared, Millimeter, and Terahertz waves (IRMMW-THz) (2016). DOI 10.1109/IRMMW-THz.2016.7758538
170. Suvorov, E.V. *et al.*: Plasma Physics and Controlled Fusion **37**(11), 1207–1213 (1995). DOI 10.1088/0741-3335/37/11/002
171. Tardocchi M. *et al.*: Nucl. Fusion **42**, 1273 (2002). DOI 10.1088/0029-5515/42/10/311

172. Tardocchi, M. *et al.*: Physical Review Letters **107**(20), 205,002 (2011). DOI 10.1103/PhysRevLett.107.205002
173. Tardocchi, M. *et al.*: Plasma Physics and Controlled Fusion **55**(7), 074,014 (2013). DOI 10.1088/0741-3335/55/7/074014
174. Van Zeeland, M.A. *et al.*: Nuclear Fusion **46**(10), S880 (2006). DOI 10.1088/0029-5515/46/10/S03
175. Van Zeeland, M.A. *et al.*: Nuclear Fusion **50**(8), 084,002 (2010). DOI 10.1088/0029-5515/50/8/084002
176. VanDevender B.A. *et al.*: IEEE Trans. Nucl. Sci. **61**, 2619 (2014). DOI 10.1109/TNS.2014.2357059
177. Weiland, M.: Nuclear Fusion **XX**, XXX (2017)
178. Weiland, M. *et al.*: Plasma Physics and Controlled Fusion **58**(2), 025,012 (2016). DOI 10.1088/0741-3335/58/2/025012
179. Werner, A. *et al.*: Review of Scientific Instruments **72**(1), 780–783 (2001). DOI 10.1063/1.1319357
180. Wong, K. L. *et al.*: Phys. Rev. Lett. **66**, 1874–1877 (1991). DOI 10.1103/PhysRevLett.66.1874
181. Woskoboinikow, P. *et al.*: International Journal of Infrared and Millimeter Waves **4**(2), 205–229 (1983). DOI 10.1007/BF01008603
182. Yamaguchi, Y. *et al.*: Nuclear Fusion **55**(1), 013,002 (2015). DOI 10.1088/0029-5515/55/1/013002
183. Zhang X. *et al.*: Nucl. Fusion **54**, 104,008 (2014). URL 10.1088/0029-5515/54/10/104008
184. Zhang X. *et al.*: Rev. Sci. Instrum. **85**, 043,503 (2014). DOI 10.1063/1.4869804
185. Zimbal A. *et al.*: Rev. Sci. Instrum. **75**, 3553 (2004). DOI 10.1063/1.1787935
186. Zweben, S.J. *et al.*: Nuclear Fusion **35**(12), 1445 (1995). DOI 10.1088/0029-5515/35/12/I04
187. Zweben, S.J. *et al.*: Nuclear Fusion **39**(9), 1097 (1999). DOI 10.1088/0029-5515/39/9/304